Materials and Design 182 (2019) 108057

Contents lists available at ScienceDirect

Materials and Design

journal homepage: www.elsevier.com/locate/matdes

# Nonlinear elastic finite fracture mechanics: Modeling mixed-mode crack nucleation in structural glazing silicone sealants

P.L. Rosendahl[a,*], Y. Staudt[b], A.P. Schneider[a], J. Schneider[c], W. Becker[a]

[a]Technische Universität Darmstadt, Fachgebiet Strukturmechanik, Franziska-Braun-Str. 7, Darmstadt 64287, Germany
[b]Ingenieurbüro Bräuer und Späh, Ludwig-Beck-Str. 8, Mannheim 68163, Germany
[c]Technische Universität Darmstadt, Institute of Structural Mechanics and Design, Franziska-Braun-Str. 3, Darmstadt 64287, Germany

## HIGHLIGHTS

- A physically sound model for crack nucleation in nonlinear elastic materials is presented
- The constitutive and bulk failure behavior of a hyperelastic material is characterized using a large set of experiments
- The proposed coupled strain and energy failure criterion is validated using several independent tests of notched specimens
- Crack nucleation, unstable crack growth, crack arrest and subsequent stable crack growth are observed in video recordings
- An anaylsis of nonmonotonic energy release rates explains and predicts the observed crack growth characteristics

## GRAPHICAL ABSTRACT

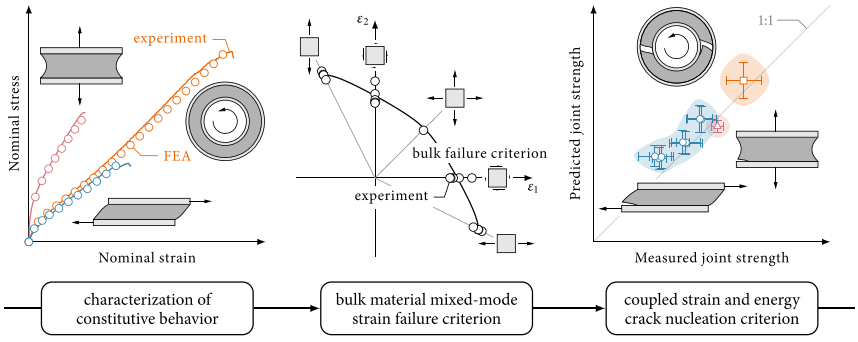


## ARTICLE INFO

*Article history:*
Received 24 April 2019
Received in revised form 17 July 2019
Accepted 18 July 2019
Available online 3 August 2019

*Keywords:*
Hyperelasticity
Finite fracture mechanics
Crack nucleation
Crack arrest
Mixed-mode
Negative geometry

## ABSTRACT

Requiring both stress and energy conditions to be met simultaneously proved key to modeling brittle crack formation at singular and nonsingular stress concentrations in linear elastic materials. The present work extends this so-called coupled stress and energy criterion to brittle crack nucleation in hyperelastic media using the example of silicone adhesives. For this purpose, we provide a comprehensive constitutive as well as fracture mechanical characterization of the structural silicone adhesive DOWSIL™ 993 using a large set of experiments and propose a mixed-mode failure model for crack initiation in nonlinear elastic materials. Characterized in independent experiments, the model is used to determine critical loads of hyperelastic adhesive bonds in both shear and tension dominated configurations. For any of the examined adhesive joint configurations the model predicts and explains size effects and agrees well with experimental findings. We study stable and unstable crack propagation observed in video recordings of our experiments. It is shown that crack initiation, crack growth and crack arrest are caused by nonmonotonic energy release rates and can be predicted. Effects of excess energy available after crack nucleation and initial unstable crack growth are discussed.



* Corresponding author.
*E-mail address:* rosendahl@fsm.tu-darmstadt.de (P.L. Rosendahl).

https://doi.org/10.1016/j.matdes.2019.108057

## 1. Introduction

The unique molecular structure of silicones provides mechanical properties which render them excellent structural adhesives. Silicones are amorphous cross-linked elastomers with strong silicon-oxygen backbones. Their glass transition temperature lies well below ambient temperatures which allows for considerable segmental motion at ambient conditions. Silicones typically exhibit hyperelastic behavior, high failure strain, low elastic modulus, excellent adhesion to many materials and a good resistance to environmental impacts and aging. When used as adhesives, silicones transfer loads homogeneously and can compensate for large deformation differences between adherends originating, e.g., from thermal mismatch. However, at bi-material corners between adherends and adhesive stress singularities owing to geometrical and material discontinuities are present. In order to capture crack onset at these singularities, classical approaches such as stress-based criteria or fracture mechanics can only be applied using an additional length parameter.

In fact, many modern theories of fracture involve a material length scale, i.e., a parameter with the dimensions of a length. Some models use physically motivated lengths, for instance derived from the microstructure or the length of a crack increment. Others involve length scales implicitly, for instance as the size of fracture process zones. Models using length scales explicitly are known under the common name theory of critical distances (TCD). Among these nonlocal approaches there are stress-based methods such as point method (PM) and line method (LM) where stresses are evaluated either in a point-wise manner in a certain distance from a stress concentration [1,2] or averaged over a specific length [3]. Nonlocal approaches using fracture mechanics are the imaginary crack method (ICM) which examines the energy release rate at the tip of an assumed pre-existing crack [4] and the finite crack extension method (FCE) which averages the energy release rate over a finite crack extension [5]. Strain energy density (SED) methods either evaluate SED along rays from the crack tip [6] or averaged in a finite sized domain [7]. A comprehensive review on SED methods is given by Berto and Lazzarin [8] and a detailed discussion on TCD by Taylor [9].

Phase-field models for brittle fracture include a regularization length which is often interpreted as a material parameter. Based on Griffith's idea of competition between elastic and fracture energy and its variational formulation by Francfort and Marigo [10], phase-field models are able to predict propagation of existing cracks, crack branching and crack paths. However, critical loads depend on the regularization parameter. Recent works by Tanné et al. [11] and Wu and Nguyen [12] suggest that fracture processes are governed by stress and energy simultaneously. Tanné et al. [11] identify the regularization length of their phase-field approach from the material's strength. Wu and Nguyen [12] use a phase-field regularized cohesive zone model and derive the regularization length from the traction-separation law, i.e., dependent on both strength and toughness. Considering strength and toughness simultaneously both works are capable of modeling not only crack propagation but also initiation using the phase-field approach. In process zone models such as cohesive zone models (CZMs) the size of the process zone appears as an implicit length scale [13,14]. In CZMs, local damage initiation is governed by the material's strength. Damage evolution is described using traction-separation laws relating crack opening displacements to stresses acting on the crack surface. The work done by tractions during the material softening process in the cohesive zone corresponds to the fracture toughness. Peridynamics contains the so-called horizon, i.e., the cut-off length of interparticle interactions as a length scale [15].

Different nonlocal approaches were successfully applied to hyperelastic materials. Clift et al. [16] and Hagl [17] evaluate stress criteria in relatively coarsely discretized finite element analyses (FEAs) of silicone bonds. Using a fixed discretization in FEAs introduces the element size as a characteristic length scale implicitly. Ayatollahi et al. [18] and Heydari-Meybodi et al. [19] are more specific in their use of a critical distance in rubbers. They evaluate an effective stretch criterion in a certain distance from notches and obtain good agreements with experiments. Berto [20] and Heydari-Meybodi et al. [21] average strain energy density (SED) in a finite volume around V-notches to predict crack initiation. Schänzel et al. [22] and Miehe and Schänzel [23] predict crack initiation in hyperelastic materials using the regularized phase-field approach. The models are able to describe experimental findings on hyperelastic materials adequately. Yet, the length parameter involved in all of the above approaches is not known a priori and lacks definite physical meaning. Pipes et al. [24] for instance, find a dependence of the critical distance on geometrical features which, hence, cannot be regarded a material constant.

Assuming the sudden nucleation of a finite sized crack introduces a length scale with clear physical meaning – the finite size of the initiated crack. The concept is known as finite fracture mechanics (FFM) and was suggested by Hashin [5]. In order to determine the finite crack size Leguillon [25] proposed requiring the simultaneous satisfaction of both a stress and an energy criterion as necessary and sufficient condition for crack nucleation. This so-called coupled stress and energy criterion involves two equations which allow for computing two unknowns: the critical loading and the size of the initiating crack. The coupled criterion requires only the fundamental material properties strength and fracture toughness as inputs. It provides excellent predictions for the failure of structures with sharp [26,27] and rounded [28] notches or round and elliptical open-holes [29,30]. It can describe mixed-mode failure [31,32], cracks through interfaces [33], adhesive joint failure [34–37], bolted joint failure [38], thermo-mechanical problems [39], the formation of crack patterns [40,41], transverse cracking of cross-ply laminates [42,43], free-edge delamination [44], 3D crack initiation [45,46] and can be linked to micromechanical material properties [47]. A comprehensive review is given by Weißgraeber et al. [48].

Common to all of the above FFM studies are the assumptions of brittleness and linear-elastic material behavior. However, the physical background of the coupled criterion allows for a generalization of the method. For instance, Leguillon and Yosibash [49] develop a theoretical FFM framework for quasi-brittle materials. The present work proposes a formulation of finite fracture mechanics for hyperelastic materials. It uses the example of structural silicone adhesives. Yet, the presented methodology is applicable to crack initiation from stress concentrations in any nonlinear elastic material.

The present work demonstrates how a physical understanding of the failure processes in complex materials allows for predicting critical loads as well as crack nucleation, crack propagation and crack arrest. It is organized as follows. Section 2 derives a mixed-mode failure model for nonlinear elastic media. Section 3 is dedicated to the constitutive and fracture mechanical characterization of the silicone adhesive examined throughout this work. Section 4 discusses failure processes observed in hyperelastic adhesive bonds. It examines conditions for crack initiation as well as crack growth, crack arrest and ultimate failure.

## 2. Failure model for brittle crack nucleation in hyperelastic materials

Modeling crack nucleation from notches in incompressible hyperelastic media is challenging for several reasons: i) Notches induce weak singularities with infinite stresses but vanishing energy release rates, ii) the onset of interface cracks is a mixed-mode fracture problem and iii) nonlinear elastic constitutive behavior must be accounted for. In order to address all of the above points let us consider DOWSIL™ 993 (previously known as Dow Corning® 993) as an example. DOWSIL™ 993 is a nearly incompressible hyperelastic two-component room temperature curing silicone. Despite large

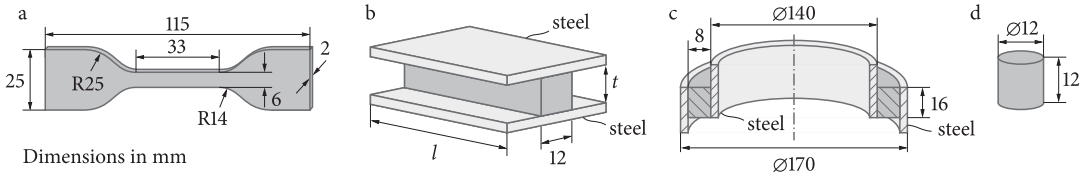


**Fig. 1.** DOWSIL™ 993 specimens used in the present work. a) Dumbbell specimen for uniaxial tests according to ASTM Standard D412-16 [50], b) H-shaped specimen with adhesive thickness $t$ and bond length $l$ for simple shear and normal plate separation tests according to ETAG 002 [51], c) tubular lap joint specimen for unnotched circular shear tests and d) cylindrical specimen for uniaxial compression tests according to ISO 7743 [52]. Please refer to Staudt et al. [53] for details on specimen manufacturing.

deformations prior to failure, no significant zone of inelastic deformations develops. Fracture surfaces of a fully fractured specimen align perfectly because only the formation of the fracture surface dissipates energy. The specimen will take its original shape when put back together because no inelastic processes occur. Hence, fracture of DOWSIL™ 993 is associated to a sudden drop in loading and can be considered brittle.

Using the specimens shown in Fig. 1 we characterize the constitutive behavior of DOWSIL™ 993 and develop a strain-based mixed-mode failure criterion for the hyperelastic bulk material. Separate fracture toughness measurements together with this bulk material failure criterion allow for the derivation of a coupled strain and energy failure model for corner-induced crack nucleation in notched specimens such as illustrated in Fig. 2. We employ finite fracture mechanics because of its simplicity, its advantages for the modeling of interface cracks and mode mixity and because of the definite physical meaning of the length scale involved.

### 2.1. Finite fracture mechanics

Leguillon [25] showed that fracture processes are governed not by one exclusive but by two conditions simultaneously, even if one often hides the other. The failure of an isotropic homogeneous bar subjected to tensile loading is dominated by stress or strain, respectively. Evaluating a stress or strain criterion provides accurate failure predictions and energy seems irrelevant. The growth of existing cracks is dominated by energy. It can be assessed evaluating the Griffith criterion

$$G = -\frac{\mathrm{d}\Pi}{\mathrm{d}A} = G_\mathrm{c}, \tag{1}$$

where $G$ denotes the differential energy release rate, $\Pi$ the total potential energy of the structure, $A$ is the surface area of the crack and $G_\mathrm{c}$ the fracture toughness. No consideration of stress or strain is required. However, the bi-material notch between adherends and adhesive is a weak singularity [34]. Stresses and strains are infinite yet the differential energy release rate vanishes. Evaluating a pure stress or strain criterion locally at the bi-material point would predict failure at any given loading. The Griffith criterion Eq. (1) can never be satisfied, i.e., it predicts infinite failure loads. This contradiction is resolved considering both conditions as necessary conditions and only their simultaneous satisfaction as a sufficient condition for crack nucleation. The concept is known as finite fracture mechanics and uses the so-called coupled stress and energy criterion proposed by Leguillon [25]. It assumes the instantaneous formation of a crack of finite size $\Delta A$ when both a stress and an energy criterion are satisfied simultaneously. As we will discuss in Section 3.2, the present work replaces the stress criterion of classical FFM by a strain criterion to accurately describe mixed-mode failure of nonlinear elastic materials.

Assuming the instantaneous formation of a finite sized crack at a critical load requires the determination of two unknowns: the failure load $P_\mathrm{f}$ and the size of the nucleating crack $\Delta A$. For this purpose, the coupled criterion requires the simultaneous satisfaction of two necessary conditions: The structure must be overloaded in a finite domain and the energy release of a finite crack must suffice. The energy condition requires the incremental energy release rate to exceed the material's fracture toughness

$$\bar{G}(\Delta A) \geq G_\mathrm{c}, \tag{2}$$

where the incremental energy release rate $\bar{G}$ for a crack increment of surface area $\Delta A$ is defined as

$$\bar{G}(\Delta A) = \frac{1}{\Delta A}\int_{\Delta A} G(\tilde{A})\mathrm{d}\tilde{A} = -\frac{\Delta\Pi}{\Delta A}, \tag{3}$$

with the change in total potential energy of the structure $\Delta\Pi$. In the present work, we require the nonlinear elastic adhesive to be overloaded in terms of strain (see also Section 3.2). An equivalent strain

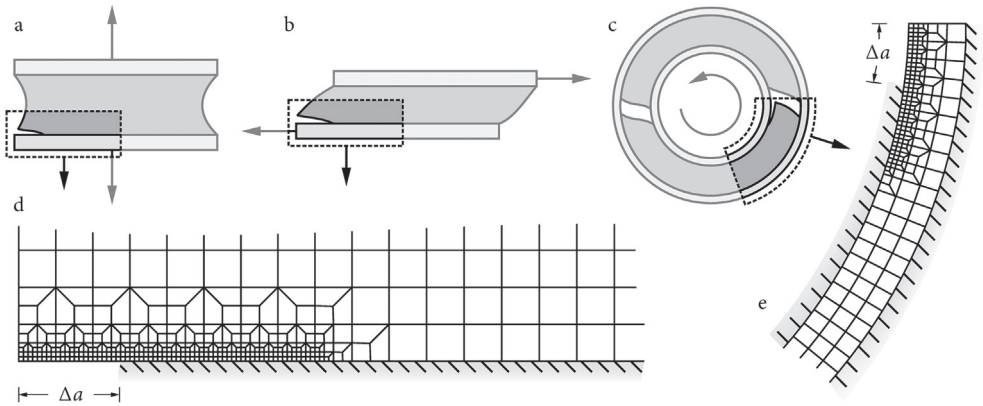


**Fig. 2.** Boundary conditions for a) normal plate separation, b) simple shear and c) notched circular shear finite element models with corresponding discretizations shown in d) and e). Adherends are modeled as rigid bodies represented by displacement boundary conditions. Cracks $\Delta a$ are modeled by partially releasing displacement constraints on silicone boundaries. The smallest element dimension is 0.1 mm.

averaged over the entire potential crack surface $\bar{\varepsilon}_{\mathrm{eq}}(\Delta A)$ must exceed a critical threshold

$$\bar{\varepsilon}_{\mathrm{eq}}(\Delta A) = \frac{1}{\Delta A}\int_{\Delta A} \varepsilon_{\mathrm{eq}}(x)\mathrm{d}A \geq \varepsilon_{\mathrm{c}}. \tag{4}$$

The chosen equivalent strain function $\varepsilon_{\mathrm{eq}}$ must be capable of describing bulk material failure under complex loads at any given location $x$. Please note that instead of averaging the equivalent strain function on the potential crack surface, we may also simply require it to be exceeded in every point of the crack surface. The former is known as line method, the latter as point method. A discussion of their differences shall be omitted in the present work. We use the equivalent strain function

$$\varepsilon_{\mathrm{eq}}(x) = \sqrt{2I_2'(x)}\cos\left[\beta\frac{\pi}{6} - \frac{1}{3}\arccos\left(\alpha\,\frac{3\sqrt{3}}{2}\,\frac{I_3'(x)}{I_2'(x)^{3/2}}\right)\right], \tag{5}$$

where $\alpha$ and $\beta$ are shape parameters and $I_2'$ and $I_3'$ deviatoric invariants of the Hencky strain tensor, see Appendix A and Eqs. (A.5) and (A.6). For plane problems with through-thickness cracks and out-of-plane width $w$ we obtain $\Delta A = w\Delta a$ and the coupled criterion reads

$$\bar{\varepsilon}_{\mathrm{eq}}(\Delta a) \geq \varepsilon_{\mathrm{c}} \quad \wedge \quad \bar{G}(\Delta a) \geq G_{\mathrm{c}}. \tag{6}$$

Cracks within adhesives, which often constitute the weakest link in complex structures, are forced onto certain paths prescribed by the shape of adherends and adhesive. Hence, crack initiation in adhesive bonds is a mixed-mode problem which the strain criterion Eq. (4) accounts for. However, concerning mode mixity of the energy criterion, no measurements of the mode II fracture toughness $G_{\mathrm{IIc}}$ are available for DOWSIL™ 993. Therefore, we may assume the equality of $G_{\mathrm{c}} = G_{\mathrm{Ic}}$ in Eq. (2). Since for most engineering materials the mode II fracture toughness is larger than the mode I fracture toughness, $G_{\mathrm{IIc}} > G_{\mathrm{Ic}}$, this is a conservative assumption.

### 2.2. Computation of logarithmic strains and energy release rates

True (logarithmic) strains and incremental energy release rates required as inputs for the present failure criterion, Eq. (6), are computed using the commercial finite element analysis (FEA) software Abaqus®. Crack nucleation in three different test geometries (Fig. 2) is examined. The H-shaped specimen shown in Fig. 1b is tested in tension (Fig. 2a) and simple shear (Fig. 2b) until failure. Additionally, notched versions (Fig. 2c) of the tubular lap joint shown in Fig. 1c are tested in a circular shear setup. Notches are manufactured by inserting 3 mm thick PTFE plates prior to pouring the silicone. The finite element discretization of the different test geometries is shown in Fig. 2d and e. Because of the strong elastic contrast between the silicone adhesive with an initial Young's modulus at the order of 1 MPa and steel adherends with a Young's modulus at the order of 200 GPa, the adherends are modeled rigid. Cracks $\Delta a$ are introduced by locally removing displacement constraints from the adhesive boundary. This yields the following boundary-value problem

$$\begin{cases} -\mathrm{div}\,\boldsymbol{\sigma} = 0 & \text{in} \quad \Omega, \\ \boldsymbol{u} = 0 & \text{along} \quad \Gamma_0, \\ \boldsymbol{u} = \boldsymbol{u}^* & \text{along} \quad \Gamma_{\mathrm{u}}, \\ \boldsymbol{\sigma}\cdot\boldsymbol{n} = 0 & \text{along} \quad \Gamma_- \cup \Gamma_+ \cup \Gamma_{\mathrm{a}}, \end{cases} \tag{7}$$

where $\boldsymbol{\sigma}$ is the Cauchy stress tensor, $\boldsymbol{u}$ the displacement vector field, $\boldsymbol{n}$ the unit outward normal vector and $\partial\Omega = \Gamma_{\mathrm{a}} \cup \Gamma_0 \cup \Gamma_+ \cup \Gamma_{\mathrm{u}} \cup \Gamma_-$ the boundary of the problem domain $\Omega$ (Fig. 3). We prescribe stress-free boundary conditions along $\Gamma_-$ and $\Gamma_+$, vanishing displacements along $\Gamma_0$ and constant displacements $\boldsymbol{u}^*$ along $\Gamma_{\mathrm{u}}$. Cracks are represented by the stress-free boundary $\Gamma_{\mathrm{a}}$. In experiments we observe cohesive cracks which nucleate from the singular bi-material notch and grow close to the interface within the adhesive. Using bulk adhesive fracture properties for the failure criterion, cohesive failure can be examined despite modeling cracks geometrically within the adherend-adhesive interface. Introducing cracks within or close to the interface has an insignificant impact on failure load predictions as shown by Hell et al. [35].

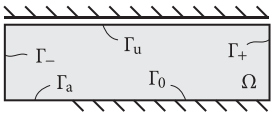


**Fig. 3.** Schematic representation of the considered boundary-value problems. The boundaries $\Gamma_-$ and $\Gamma_+$ are stress-free. Along $\Gamma_0$ we prescribe vanishing displacements and along $\Gamma_{\mathrm{u}}$ constant (horizontal) displacements. Cracks are represented by the stress-free boundary $\Gamma_{\mathrm{a}}$.

The hyperelastic adhesive is modeled using the Marlow material model detailed and characterized in Section 3.1. It is assumed fully incompressible and its Poisson's ratio set to $\nu = 0.5$. Four-noded Abaqus plane-strain hybrid elements with selective reduced pressure integration are used. Specimens are loaded by prescribed displacements. Converged discretizations structured as shown in Fig. 2 have less then 10 000 degrees of freedom. Solving a single nonlinear boundary value problem requires less then 30 s on a standard desktop computer. For immediate visualization of the mixed-mode strain hypothesis, Eq. (5), the user subroutine provided by Rosendahl et al. [54] can be used.

The adhesive is loaded by prescribed vertical, horizontal or circular displacements, respectively. External work vanishes and the total potential energy equals the stored strain energy $\Pi = \Pi^{\mathrm{i}}$. Incremental energy release rates are computed from the difference in stored strain energy $\Pi^{\mathrm{i}}$ between cracked and uncracked configurations

$$\bar{G}(P,\Delta a) = -\frac{\Pi_1^{\mathrm{i}}(P,\Delta a) - \Pi_0^{\mathrm{i}}(P)}{w\Delta a}, \tag{8}$$

where the subscripts 0 and 1 correspond to the uncracked and cracked state, respectively, $P$ denotes the external (reaction force) loading, $\Delta a$ is the crack length and $w$ the out-of-plane specimen width.

### 2.3. Optimization problem and performance

Solving the coupled criterion, Eq. (6), results in a constrained optimization problem where the smallest load $P$ satisfying both the strain and the energy criterion, Eqs. (2) and (4), is to be found for any kinematically admissible crack $\Delta a$:

$$P_{\mathrm{f}} = \min_{P,\Delta a} \{P \mid P > 0, \exists\, \Delta a > 0 : \bar{\varepsilon}_{\mathrm{eq}}(P,\Delta a) \geq \varepsilon_{\mathrm{c}} \quad \wedge \quad \bar{G}(P,\Delta a) \geq G_{\mathrm{c}}\}. \tag{9}$$

If $\bar{\varepsilon}_{\mathrm{eq}}(P,\Delta a)$ and $\bar{G}(P,\Delta a)$ are monotonic with respect to $\Delta a$, the optimization problem can be solved using an iterative algorithm, see e.g. Felger et al. [55]. The iterative scheme computes equivalent strain and incremental energy release rate repetitively to update load and crack length accordingly.

In the present case, the energy release rate is not monotonic which is typical for adhesive joints [56] and requires an online-offline strategy. In the online stage, equivalent strain function and energy release rate are evaluated on a grid of feasible crack lengths and loads. In order to provide $\bar{G}(P,\Delta a)$ in adequate resolution, the load

is applied in at least 20 increments and cracks are resolved in 32 to 96 increments depending on their estimated maximum length. In the offline stage, $\bar{\varepsilon}_{eq}(P, \Delta a)$ and $\bar{G}(P, \Delta a)$ are interpolated on the grid using bicubic splines. Critical load and length of the initiating crack are then determined using the sequential least squares programming algorithm of the scientific computing Python library SciPy. Computing the online stage dataset for one particular specimen geometry requires a few minutes on a standard desktop computer. Interpolating the data and solving for failure load and crack length in the offline stage takes less than 100 ms.

## 3. Material characterization

The characterization of hyperelastic adhesives is challenging because of their incompressibility, high failure strain and low elastic modulus. It requires thorough validation of derived properties. We determine the constitutive behavior of DOWSIL™ 993 using dumbbell shaped bulk specimens and validate the material model using different bonded specimens (Fig. 1). A bulk material failure criterion is developed using uniaxial tension (Fig. 1a), circular shear (Fig. 1c) and uniaxial compression tests (Fig. 1d). Fracture toughness measurements are taken from literature.

### 3.1. Constitutive behavior

Fig. 1 shows specimens used for material characterization and throughout the present work. Dumbbell specimens for uniaxial tensile tests (Fig. 1a) are manufactured by pouring a sheet of DOWSIL™ 993 of 2 mm nominal thickness onto a polyethylene (PE) foil. The sheets are stored at ambient conditions for one week before specimens are punched and tested at 23 °C and 50% relative humidity. For all other specimens polytetrafluoroethylene (PTFE) or PE moulds are used. The steel adherends for H-shaped and tubular specimens (Fig. 1b and c) are sandblasted, ground, carefully cleaned with DOWSIL™ R-40 cleaner and primed with DOWSIL™ 1200 OS primer prior to pouring the adhesive. Adhesive specimens are stored for four weeks at ambient conditions before testing. Silicone mixing and pouring for all specimens is performed using a professional static mixing and dispense pump. Details on specimen manufacturing and test methods are reported by Staudt et al. [53].

The constitutive behavior of DOWSIL™ 993 is determined in uniaxial tensile tests according to ASTM Standard D412-16 [50]. True strain is measured using digital image correlation (DIC). True stress is computed from the force signal considering the change of the cross section during loading. Fig. 4a shows measurements of five specimens reported by Staudt et al. [53]. Assuming incompressibility, i.e., Poisson's ratio $\nu = 0.5$, the smoothed mean of all five measurements is used as tabular input for a Marlow-type material model. This material model assumes a dependence of the strain energy density on the first invariant of the left Cauchy-Green strain tensor only. Under this assumption, it derives a constitutive relation equating the first invariant of complex deformation states and the first invariant of deformation states in uniaxial tensile tests. Thus, it requires no parameter identification but uses uniaxial tension data as input directly. Using the tabular data of Fig. 4a, experiments of different adhesive specimens are reproduced using finite element analyses (FEAs) in Fig. 4b. Simple shear and normal plate separation tests using the H-shaped specimen (Fig. 1b) and a circular shear test using the tubular lap joint specimen (Fig. 1c) are shown. The Marlow material model provides an excellent description of the constitutive behavior of DOWSIL™ 993 in all tested configurations.

### 3.2. Bulk material failure

Typically, adhesive joint fracture is a mixed-mode problem which requires the determination of mixed-mode fracture properties. Staudt et al. [53] report strength measurements of DOWSIL™ 993 in uniaxial tension, uniaxial compression and circular shear. However, as shown by Rosendahl et al. [54], failure of nonlinear materials is more accurately and robustly described in terms of ultimate extensibility. In the following, the experiments of Staudt et al. [53] are re-evaluated with respect to ultimate true strains to derive a mixed-mode failure hypothesis as suggested by Rosendahl et al. [54]. Table 1 lists the failure data of the experiments of Staudt et al. [53] evaluated in terms of ultimate principal true strains. It comprises uniaxial tension (see Fig. 1a), circular shear (see Fig. 1c) and uniaxial compression (see Fig. 1d) tests. The strain state in uniaxial compression is equivalent to the equibiaxial tension strain state for an incompressible material such as DOWSIL™993.

Isotropic materials may exhibit two distinct failure modes [58]. For nearly incompressible materials such as silicones, these two failure modes are directly associated to distortional and dilatational deformations, respectively [59,60]. Silicone adhesives are typically applied as thick glue beads with rectangular cross section (cf. Fig. 1). Their volumetric constraint is weak and volume change is fairly unrestricted. Hence, failure of thick adhesive bonds is dominated

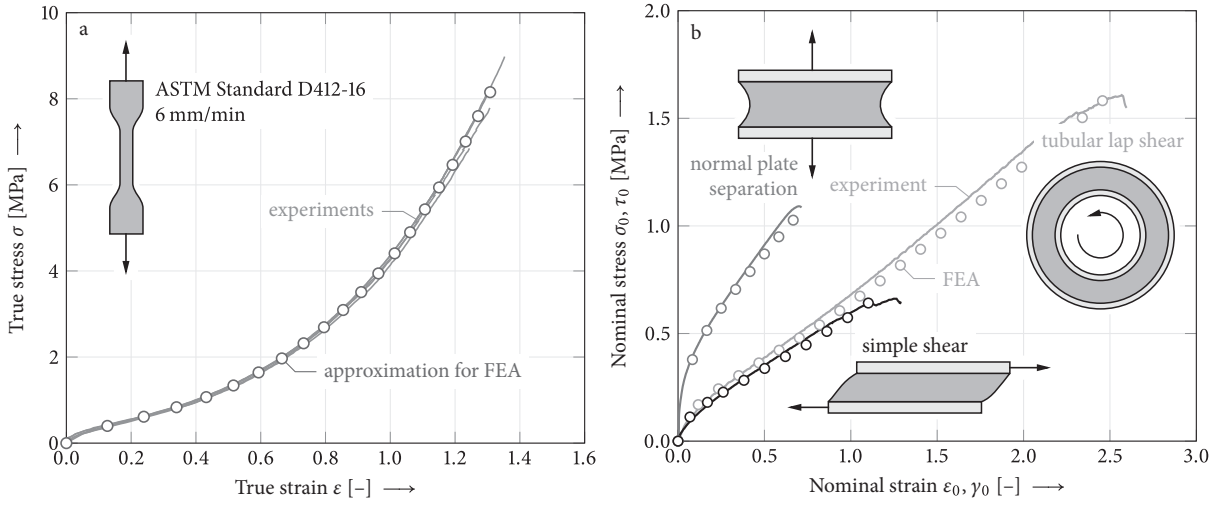


**Fig. 4.** Characterization of the constitutive behavior of DOWSIL™ 993. a) Uniaxial tension test according to ASTM Standard D412-16 [50] used as tabular input for a Marlow-type finite element analysis (FEA) material model. b) Numerical reproduction using FEAs of different adhesive joint geometries studied in the present work using the Marlow material model. Experimental data taken from Staudt et al. [53] for uniaxial tension, simple shear and tubular lap shear tests and Staudt [57] for the normal plate separation test.

**Table 1**
Ultimate principal true strains of DOWSIL™ 993 in experiments reported by Staudt et al. [53] and Rosendahl et al. [54].

| Test setup | $\varepsilon_1$ | $\varepsilon_2$ | $\varepsilon_3$ |
|---|---|---|---|
| Uniaxial tension | 1.353 | −0.675 | −0.675 |
| | 1.304 | −0.652 | −0.652 |
| | 1.311 | −0.655 | −0.655 |
| | 1.307 | −0.654 | −0.654 |
| | 1.244 | −0.622 | −0.622 |
| Circular shear | 1.066 | 0.0 | −1.076 |
| | 1.226 | 0.0 | −1.255 |
| | 0.949 | 0.0 | −0.958 |
| | 0.990 | 0.0 | −0.999 |
| | 0.958 | 0.0 | −0.967 |
| Uniaxial compression | 0.614 | 0.603 | −1.217 |

by distortion. The relevance of dilatational failure modes can be estimated from the ratio of free to bonded surface area of the adhesive. For adhesive beads with rectangular cross section this ratio is expressed approximately by the ratio of thickness to out-of-plane width $t/w$. The smallest aspect ratio $t/w = 1/2$ tested in the present work falls in-between two aspect ratios where Aït Hocine et al. [61] observe a transition from cavitation to no cavitation in tensile tests of flat circular adhesive joints. Cavities which form during loading can be easily identified on fracture surfaces [see 61]. However, fracture surfaces of specimens examined in the present work showed no sign of cavitation. Hence, a discussion of dilatational failure can be excluded from the present study, see also Drass et al. [62,63].

Multi-axial failure can be described mathematically by a surface $\Phi$ in principal strain space which comprises all deformation states associated to failure. According to the corresponding failure criterion

$$\Phi(\boldsymbol{H}) = 0, \tag{10}$$

a material can sustain deformations when $\Phi(\boldsymbol{H}) < 0$ and will fail when it reaches $\Phi(\boldsymbol{H}) = 0$ (or hypothetically $\Phi(\boldsymbol{H}) > 0$). Here, $\boldsymbol{H}$ denotes the true strain spatial Hencky strain tensor, see Appendix A. For practical use, a function which allows for comparing arbitrary states of deformation to a scalar threshold value is needed. For this purpose, an equivalent strain function $\varepsilon_{\mathrm{eq}}(\boldsymbol{H})$ transforming the tensor-valued input $\boldsymbol{H}$ into a scalar quantity may be introduced. Comparing the equivalent strain against its critical value $\varepsilon_{\mathrm{c}}$, yields a description of the failure surface

$$\Phi(\boldsymbol{H}) = \varepsilon_{\mathrm{eq}}(\boldsymbol{H}) - \varepsilon_{\mathrm{c}} = 0. \tag{11}$$

Deformation states $\boldsymbol{H}$ coincide with the failure surface when $\varepsilon_{\mathrm{eq}}/\varepsilon_{\mathrm{c}} = 1$. As shown by Rosendahl et al. [54], an equivalent strain function of the form

$$\varepsilon_{\mathrm{eq}}(\boldsymbol{H}(\boldsymbol{x})) = \sqrt{2I_2'(\boldsymbol{x})}\cos\left[\beta\frac{\pi}{6} - \frac{1}{3}\arccos\left(\alpha\,\frac{3\sqrt{3}}{2}\,\frac{I_3'(\boldsymbol{x})}{I_2'(\boldsymbol{x})^{3/2}}\right)\right], \tag{12}$$

evaluated at locations $\boldsymbol{x}$, where $\alpha \in [0,1]$ and $\beta \in [0,2]$, is well suited for the description of distortional mixed-mode failure of nearly incompressible hyperelastic media. The shape parameters $\alpha$ and $\beta$ allow for an adjustment to experimental data of many different materials [64,65]. Because only the invariants $I_2'$ and $I_3'$ of $\boldsymbol{H}_{\mathrm{dev}}$ are used (see Appendix A), Eq. (12) describes distortional failure only and we obtain $\varepsilon_{\mathrm{eq}}(\boldsymbol{H}) = \varepsilon_{\mathrm{eq}}(\boldsymbol{H}_{\mathrm{dev}})$. The equivalent strain function Eq. (12) comprises classical failure criteria in limit cases. For instance, $(\alpha,\beta) = (1,0)$ yields a (Rankine-like) maximum normal strain hypothesis, $(\alpha,\beta) = (1,1)$ yields a (Tresca-like) maximum shear strain hypothesis and for $\alpha = 0$, a von Mises-like strain criterion is obtained for any value of $\beta$. With parameters in the given intervals, the failure surface is convex.

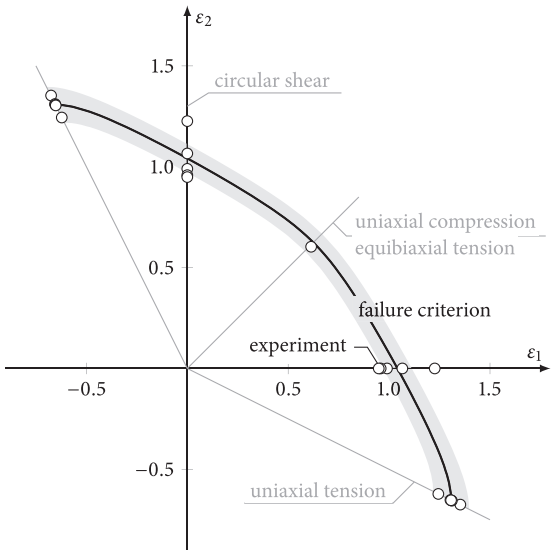


**Fig. 5.** Bulk material failure data of DOWSIL™ 993 (Table 1) in principal strain space (dots) and their approximation by the mixed-mode failure criterion, Eqs. (11) and (12), with $\varepsilon_{\mathrm{c}} = 1.47 \pm 0.10, \alpha = 0.86$ and $\beta = 1.12$ (solid line). Experimental data taken from Staudt et al. [53] and Rosendahl et al. [54].

Fig. 5 shows the failure data of Table 1 in principal strain space. Because DOWSIL™ 993 is assumed incompressible, only two principal true strains are independent, a two-dimensional representation suffices and $\varepsilon_3$ can be computed from $\varepsilon_3 = -\varepsilon_1 - \varepsilon_2$. The parameters of the failure criterion, Eqs. (11) and (12), are identified using a least squares approximation. With $\varepsilon_{\mathrm{c}} = 1.47 \pm 0.10, \alpha = 0.86$ and $\beta = 1.12$ as shown in Fig. 5 this mixed-mode failure criterion provides an excellent description of bulk failure of DOWSIL™ 993.

### 3.3. Fracture toughness

The singular nature of stress and strain fields at bi-material corners between adherends and adhesive (see e.g. Fig. 1b) renders crack nucleation at these points a combined strength-of-materials and fracture mechanics problem. It requires the identification of both a bulk material failure hypothesis and the fracture toughness.

Standardized methods to determine the fracture toughness of adhesives using adhesively bondend double cantilever beam (DCB) specimens or tapered double cantilever beam (TDCB) specimens as detailed in ASTMS tandard D3433-99 [66] or BS Standard 7991 [67] require the assumption of linearity and are not suitable for hyperelastic silicone adhesives. Based on the works of Schmandt and Marzi [68], Rosendahl et al. [69] determine the fracture toughness of DOWSIL™ 993 evaluating the path-independent J-Integral in DCB specimens bonded with the thick nonlinear elastic adhesive. They report a mode I fracture toughness of $G_{\mathrm{Ic}} = 4.22 \pm 0.60$ N/mm and remark that their J-integral-based approach may overestimate the fracture toughness by up to 13% in this particular case.

To our knowledge, the mode II fracture toughness of DOWSIL™ 993 is unknown. Assuming the equality of $G_{\mathrm{IIc}}$ and $G_{\mathrm{IIIc}}$, the test method employed by Loh and Marzi [70] may be used to determine a mode III and thus a mode II fracture toughness. However, no such measurements are known for DOWSIL™ 993. Therefore, the present work characterizes fracture toughness using $G_{\mathrm{Ic}}$ only.

**Table 2**
Mean nominal shear strength $\tau_f$ in MPa and standard deviation of 77 H-shaped of DOWSIL™ 993 specimens of nominal width $w = 12$ mm in simple shear tests. The number of tested specimens of each geometry is indicated in parentheses.

| | Adhesive thickness $t$ (# of tested specimens) | | |
|---|---|---|---|
| Length $l$ | 6 mm | 12 mm | 24 mm |
| 50 mm | $1.002 \pm 0.141$(4) | $0.855 \pm 0.153$(5) | $0.610 \pm 0.064$(4) |
| 100 mm | $0.989 \pm 0.117$(18) | $0.858 \pm 0.132$(21) | $0.630 \pm 0.110$(15) |
| 200 mm | – | $0.830 \pm 0.060$(5) | $0.570 \pm 0.151$(5) |

**Table 3**
Mean nominal strength and standard deviation of DOWSIL™ 993 in normal plate separation and circular shear tests.

| | Plate separation ($\sigma_f$) | Circular shear ($\tau_f$) |
|---|---|---|
| Nominal strength [MPa] | $1.150 \pm 0.055$ | $1.393 \pm 0.162$ |
| # of tested specimens | 7 | 4 |

## 4. Analysis of the fracture process

The failure model introduced in Section 2 allows for predicting critical loads as well as lengths of initiating and growing cracks in silicone adhesives. In the following, failure load and crack growth predictions of the model are discussed and compared against experimental observations. The discussion comprises destructive tests of H-shaped specimens (Fig. 1b) in normal plate separation (Fig. 2a) tests and simple shear (Fig. 2b) loading conditions as well as notched tubular lap joints (Figs. 1c, 2c) under circular shear loading.

### 4.1. Failure load predictions

Consider the results of the simple shear test series of H-shaped specimens (Fig. 1b) of adhesive thicknesses $t = 6$ mm, 12 mm and 24 mm and specimen lengths $l = 50$ mm, 100 mm and 200 mm listed in Table 2. We tested a total number of 77 specimens of nominal width $w = 12$ mm. Fig. 6 compares predictions of the FFM failure model to measured failure loads. Experimental data is indicated as mean and standard deviation. Nominal strengths are calculated from recorded failure loads using the actual adhesive width and length of individual manufactured specimens. FFM failure loads $\tau_f$ and initial crack lengths $\Delta a$ are evaluated using nominal dimensions and mean fracture properties accounting for 13% overestimation of

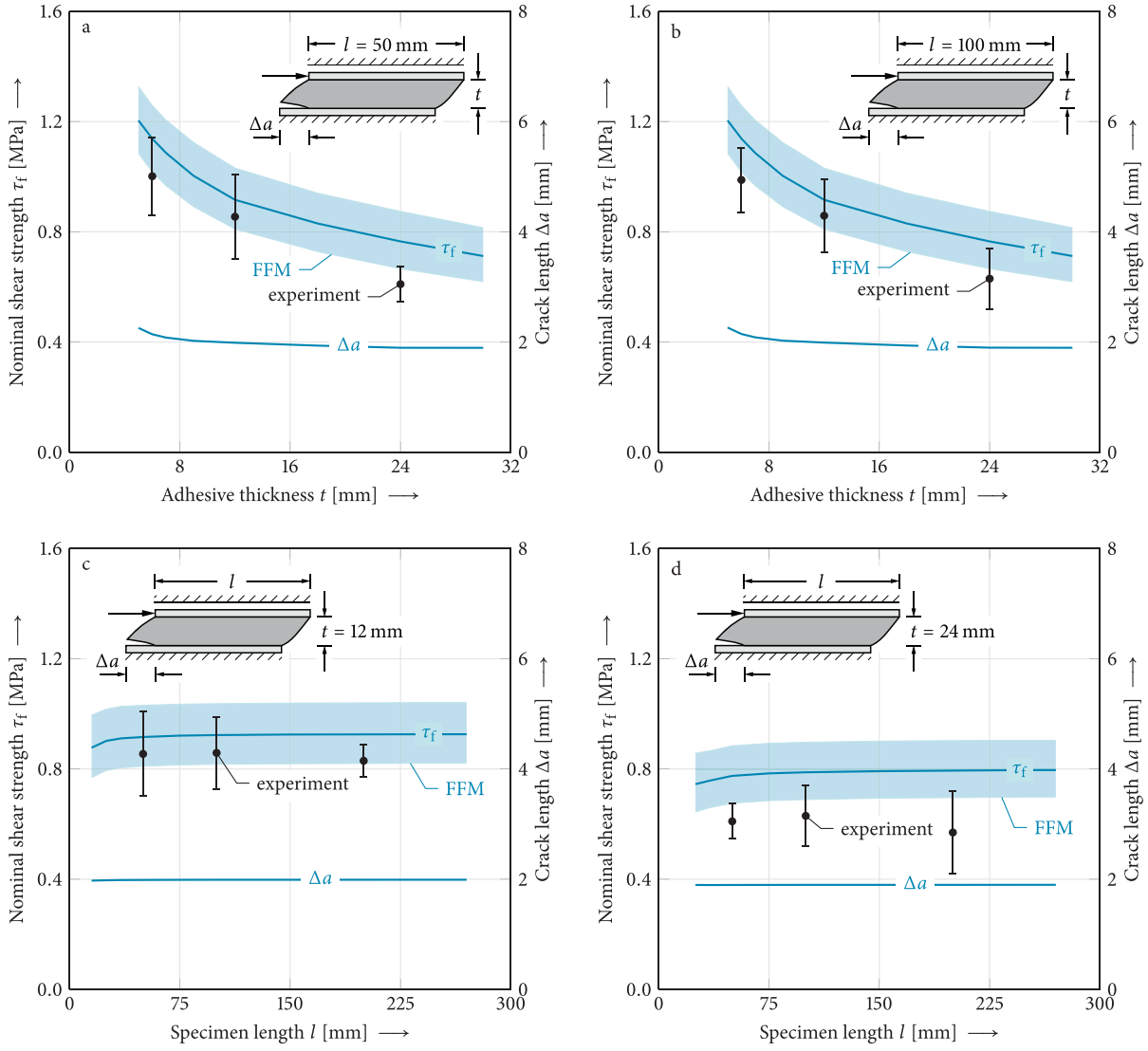


**Fig. 6.** Finite fracture mechanics (FFM) failure load predictions in comparison to experiments. The influence of adhesive thickness is shown for overlap lengths a) $l = 50$ mm and b) $l = 100$ mm. The impact of overlap length is shown for adhesive thicknesses c) $t = 12$ mm and d) $t = 24$ mm. Experimental data is indicated as mean and standard deviation. FFM failure loads $\tau_f$ are computed using mean fracture properties and given with shaded 95% confidence intervals in order to account for uncertainty of the fracture properties. Reported finite crack lengths $\Delta a$ correspond to mean fracture property predictions.

$G_c$ reported by Rosendahl et al. [69]. In order to account for the uncertainty of fracture properties, failure load predictions are given with shaded 95% confidence intervals. Overall a good agreement between model and experiments is observed despite significant scatter in both experimental data and fracture properties. While failure loads are slightly overestimated, all trends are captured correctly. Confidence intervals of the predictions overlap with experimental standard deviations in any case.

Panels a and b in Fig. 6 show the influence of adhesive thickness $t$ for overlap lengths $l = 50$ mm and $l = 100$ mm, respectively. The experiments show the adhesive thickness effect, i.e., a reduction of the effective joint strength with increasing adhesive thickness $t$. The effect originates from an increasing energy release rate with increasing adhesive thickness which dominates the crack initiation process. Because the coupled strain and energy criterion accounts for the energy balance, the effect is reproduced well. Several other studies report the adhesive thickness effect for nonlinear adhesives. For instance, Machalická and Eliášová [71] perform shear and tension tests on nonlinear polyurethane adhesive joints and Wang et al. [72] examine a two-component structural silicone in simple shear. The thickness effect suggests the use of thinner adhesive layers. However, in particular for nearly incompressible hyperelastic adhesives, a general recommendation for the application of thin adhesive layers cannot be given easily as constrained volume effects such as cavitation may occur [61]. Panels c and d in Fig. 6 show the influence of overlap length for adhesive thicknesses $t = 12$ mm and $t = 24$ mm, respectively. As expected, there is no significant increase of effective joint strength with increasing overlap length $l$ above a certain threshold. All investigated overlap lengths are as long or longer than this threshold. The model indicates threshold lengths of $l^* \approx 30$ mm for $t = 12$ mm and $l^* \approx 50$ mm for $t = 24$ mm, respectively. As observed before, the effective joint strength of the thicker adhesive is smaller. Fig 6 also shows finite crack lengths $\Delta a$ computed for mean fracture properties. Remarkably, finite crack lengths remain almost constant $\Delta a \approx 2$ mm in all geometrical configurations tested and analyzed. Panels a and b in Fig. 6 suggest they only become longer below a certain threshold adhesive thickness $t^* \leq 5$ mm. While the strain distribution in adhesive layers is only moderately affected by their adhesive thickness, the energy release rate reduces significantly with decreasing thickness. Hence, thin adhesive layers can sustain higher loads and require longer finite cracks to release sufficient energy.

In order to extend the validation of the present model to additional structural situations and load cases, consider the normal plate separation test of H-shaped specimens (Figs. 1b and 2a) and the circular shear test of notched tubular lap joints (Figs. 1c, 2c). We tested 7 H-shaped specimens with adhesive thickness $t = 12$ mm, length $l = 50$ mm and width $w = 12$ mm and 4 tubular lap joint specimens with two 3 mm notches, adhesive thickness $t = 8$ mm, width $w = 16$ mm and inner diameter ø140 mm. The results are listed in Table 3 and shown in Panels a and b in Fig. 7, respectively. Experiments are shown with mean and standard deviation. Again, FFM predictions are indicated with mean fracture properties and shaded 95% confidence intervals in order to account for uncertainty of the fracture parameters. For the plate separation tests (Fig. 7a) FFM predictions are slightly conservative. However, as observed in Fig. 6, they agree with experimental standard deviations within their confidence intervals. FFM predictions of the circular shear test (Fig. 7b) are similar to the simple shear case. While for each test setup only one geometry of the adhesive joint is tested, FFM again predicts the adhesive thickness effect which is expected to occur in the present test configurations as well. In both panels a and b in Fig. 7, remarkably constant finite crack lengths $\Delta a \approx 1.5$ mm and $\Delta a \approx 2.2$ mm computed with mean fracture properties are observed. It may be assumed that tested and analyzed adhesive thickness are again well above a threshold adhesive thickness, below which the change in finite crack length $\Delta a$ becomes pronounced.

A summary of all tested adhesive joint configurations is given in Fig. 8. It compares experimental data on the horizontal axis to FFM predictions on the vertical axis. Error bars on the horizontal axis indicate the experimental standard deviation. Error bars on the vertical axis represent predictions obtained using minimum and maximum fracture properties, respectively. Different test setups are indicated by a shaded area and their respective color. Predictions of an ideal model would collapse onto the 1-to-1-line. Predictions by the present FFM failure model are concentrated closely around this diagonal. Considering significant scatter in both the experimental data and the fracture properties, the present model may be deemed accurate for the examined hyperelastic adhesive.

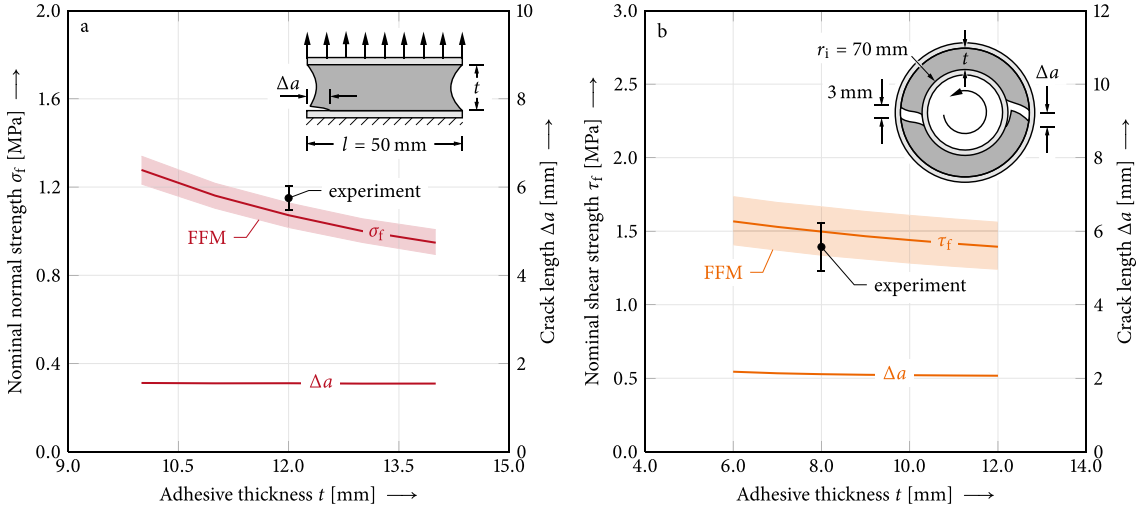


**Fig. 7.** Finite fracture mechanics (FFM) failure load predictions in comparison to a) normal plate separation tests of H-shaped specimens and b) circular shear tests of notched tubular lap joints. H-shaped specimens of length $l = 50$ mm and width $w = 12$ mm and tubular lap joints with two 3 mm notches as indicated in the pictogram, adhesive width $w = 16$ mm and inner diameter ø140 mm are examined. Experimental data is shown as mean and standard deviation. FFM predictions are computed with mean fracture properties and shown with shaded 95% confidence intervals accounting for uncertainty of the fracture properties. Computed finite crack lengths $\Delta a$ are determined using mean fracture properties.

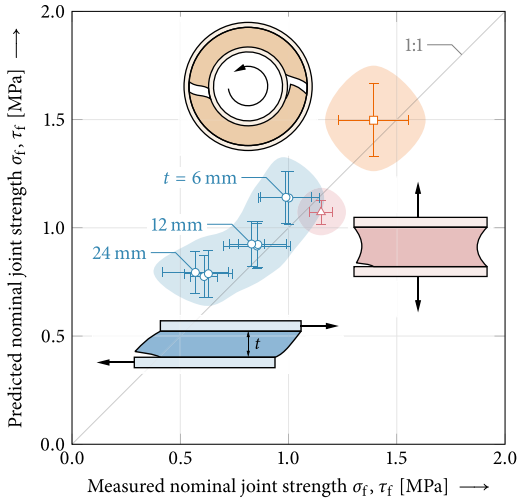


**Fig. 8.** Comparison of predicted and measured nominal strengths (initial failure) of different color-coded adhesive joints. Error bars on the horizontal axis indicate the experimental standard deviation. Error bars on the vertical axis represent predictions from minimum and maximum fracture properties, respectively. Different joint configurations are indicated by their respective color and shaded area.

### 4.2. Crack initiation, crack growth and crack arrest

In the present displacement-controlled simple shear test setup of H-shaped specimens characteristic load-displacement curves (see center column of Figs. 11 and 12) are observed consistently. Initial crack formation is not associated to ultimate failure but to a reduction and subsequent increase of the transferred load with increasing applied displacement. In order to investigate this phenomenon, we prepared video recordings of additional 12 simple shear specimens of length $l = 100$ mm. The recordings show that the phenomenon can be attributed to a nonmonotonic energy release rate, crack growth and crack arrest.

Nonmonotonic energy release rates are not unique to adhesive joints [73,35] but are found in many technical applications, often in the presence of strong elastic contrasts. Several authors study this behavior in composite laminates: Wang and Crossman [74] report it for free-edge delamination, Krueger [75] for the delamination of reinforcement patches and Martin et al. [76] for the debonding of fiber and matrix. Müller et al. [77] find nonmonotonic energy release rates for the debonding of fuel cell stacks, García et al. [78] for particle debonding in composite materials and Doitrand et al. [79] for rhombus hole specimens under quasi-static compression. Different characteristics of nonmonotonic energy release rates in different structural situations are discussed by Weißgraeber et al. [56]. Sapora and Cornetti [80] show that cracks originating from open-holes under biaxial compression may exhibit any of the characteristics discussed by Weißgraeber et al. [56] depending on the biaxiality of the loading.

In the present case the nonmonotonic behavior of the energy release rate is caused by the individual contributions of different crack opening modes to the total energy release rate. In order to separate the total energy release rate into contributions from crack opening and crack sliding modes, we model crack nucleation by the quasi-static reduction and finally removal of tractions required to hold crack flanks closed. Let us denote the work per unit crack surface done by tractions perpendicular to crack flanks during crack opening as $\bar{G}_\mathrm{I}$ and the work per unit crack surface of tangential tractions as $\bar{G}_\mathrm{II}$. This allows for splitting the total incremental energy release rate $\bar{G} = \bar{G}_\mathrm{I} + \bar{G}_\mathrm{II}$ into mode I and mode II contributions. In contrast to its linear formulation, the present nonlinear crack opening integral requires actual integration of nonlinear tractions over crack flank displacements during crack opening. As proposed by Talmon l'Armée et al. [31], we employ local nodal coordinate systems to compute crack normal and tangential tractions and displacements during crack opening.

The mode separation shown in Fig. 9 reveals that the nonmonotonic behavior of the total energy release rate is caused by crack opening mode I. $\bar{G}_\mathrm{II}$ increases monotonically with crack length while $\bar{G}_\mathrm{I}$ has a distinct maximum at comparatively short crack lengths follow by a reduction to almost zero as the crack length increases. This maximum dominates short cracks and causes the nonmonotonic behavior of the total energy release rate. Hell et al. [35] reported a similar behavior of linear elastic adhesive joints. Despite the comparison of different load levels in Fig. 9, it shall be emphasized that the energy release rate increases with increasing adhesive thickness.

When nonmonotonic energy release rates are present different scenarios for crack nucleation and for the stability of initiated cracks are possible (Fig. 10). Crack nucleation is governed by the incremental energy release rate $\bar{G}$. Whether subsequent crack propagation is stable or unstable depends on the differential energy release rate $G$. Using Eq. (3) and $\Delta A = w\Delta a$, the latter can be expressed by

$$G(\Delta a) = \bar{G}(\Delta a) + \Delta a \frac{\partial \bar{G}(\Delta a)}{\partial \Delta a}, \tag{13}$$

where $\Delta a$ is a finite crack length. Eq. (13) implies that $G$ is always larger than $\bar{G}$ where $\bar{G}$ increases ($\partial \bar{G}(\Delta a)/\partial \Delta a > 0$) and smaller where $\bar{G}$ decreases ($\partial \bar{G}(\Delta a)/\partial \Delta a < 0$). Both energy release rates coincide in local maxima or minima of $\bar{G}$ where $\partial \bar{G}(\Delta a)/\partial \Delta a = 0$. Let us denote the crack length of the first local maximum of $\bar{G}$ as $a^*$ (Fig. 10c). The crack length at which $\bar{G}$ subsequently first reaches the level of the local maximum again is denoted $a^{**}$. Initiating finite cracks $\Delta a$ shorter than $a^*$ (Fig. 10a) are initially unstable and grow without further load increase because the differential energy release rate $G$ exceeds its incremental counterpart $\bar{G}$ and thus $G_c$. Finite cracks $\Delta a = a^*$ (Fig. 10b) are stable. Here, the incremental and differential energy release rates coincide, yet the gradient of the latter is negative. The initial crack can only grow upon further load increase. Provided stresses or strains decrease monotonically, the coupled criterion, Eq. (6), does not permit finite crack nucleation between $a^*$ and $a^{**}$ (Fig. 10c). For any crack $a^* < \Delta a < a^{**}$ we could find a smaller load satisfying the energy criterion, Eq. (2), at $\Delta a = a^*$. Comparing their predictions to experimental data, Hell et al. [35] observe

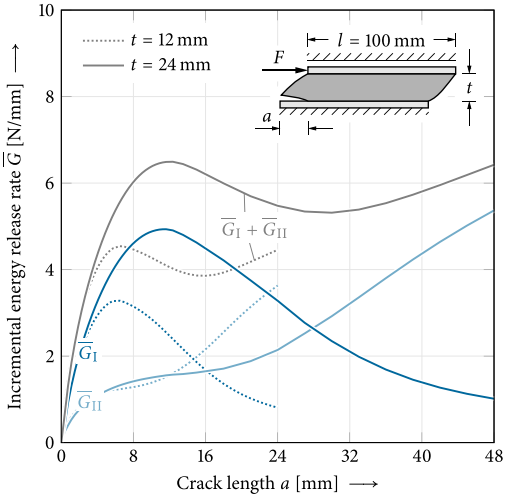


**Fig. 9.** Separation of crack opening mode I and crack sliding mode II contributions to the total incremental energy release rate $\bar{G} = \bar{G}_\mathrm{I} + \bar{G}_\mathrm{II}$ at initial failure load $F = 846$ N for specimens of adhesive thickness $t = 12$ mm and $F = 1042$ N for adhesive thickness $t = 24$ mm.

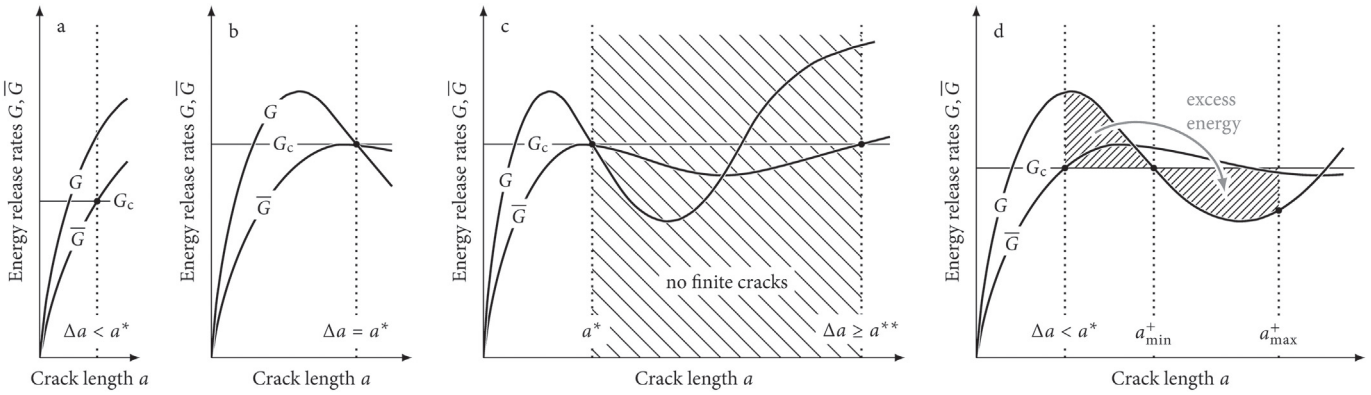


**Fig. 10.** Crack nucleation scenarios for nonmonotonic energy release rates. a) Finite cracks $\Delta a$ shorter than $a^*$ are unstable after initiation. b) Finite cracks $\Delta a = a^*$ are stable and will grow upon further load increase. c) Given a monotonically decreasing stress or strain criterion, finite fracture mechanics permits only finite cracks shorter than $a^*$ or longer than $a^{**}$. Finite cracks $\Delta a \geq a^{**}$ are again unstable after initiation. d) Nucleating cracks $\Delta a < a^*$ are unstable and will grow to $a^+_{min}$. Because $G > G_c$ during crack propagation, excess energy may be available for further crack growth up to $a^+_{max}$.

this jump in finite crack length from $a^*$ to $a^{**}$ with increasing adhesive thickness of linear elastic single-lap joints. Finite cracks longer than $a^{**}$ are again unstable and will propagate without further load increase because they are associated to a differential energy release rate $G$ which exceeds the fracture toughness $G_c$.

Given the local minimum of $G$ between $a^*$ and $a^{**}$ is smaller than $G_c$ (Fig. 10d), we observe a special situation for initially unstable cracks $\Delta a < a^*$. As they grow, they may reach a length $a^+_{min}$ at which the differential energy release rate $G$ equals the fracture toughness $G_c$. During crack propagation from $\Delta a$ to $a^+_{min}$ more energy than required for crack growth is available ($G > G_c$). Depending on the fracture dynamics and the specific structural situation, this excess energy can potentially be available for crack growth beyond $a^+_{min}$ up to $a^+_{max}$. This is also theorized by Leguillon and Martin [33,81] and Doitrand et al. [79] but experimental evidence is scarce. Weißgraeber et al. [56] introduce a parameter $\rho$ to characterize the fraction of excess energy available for crack growth beyond $a^+_{min}$.

Because Hell et al. [35] observe finite cracks longer than $a^{**}$ only for thin adhesive layers ($t < 0.8$ mm), we expect finite cracks $\Delta a \leq a*$ in the present case. Thus, crack initiation and potentially subsequent unstable crack growth are expected to cause a load drop in the present displacement controlled test setup. The magnitude of the drop depends on the local minimum of the differential energy release rate $G$ between $a^*$ and $a^{**}$. If it is larger than the fracture toughness $G_c$, immediate ultimate failure is to be expected. If it is smaller, the initial finite crack may arrest and only a finite drop in loading can be anticipated. Then, this initial load drop would be followed by stable crack growth associated to some load increase prior to ultimate failure. Figs. 11 and 12 show characteristic load-displacement curves for specimens of $t = 24$ mm and $t = 12$ mm adhesive thickness, respectively. Indeed, after an initial load drop (I–II) we observe load increase (II–III) with increasing displacement and finally ultimate failure (IV) as hypothesized above. The local minimum of $G$ is smaller than $G_c$ and stable crack growth is observed (see right columns of Figs. 11 and 12). Video recordings (snapshots in left columns of Figs. 11 and 12) show the sudden formation of a crack from the singular bi-material point at initial failure (I). Soon the crack arrests and stable growth with increasing displacement is observed (II–III), again followed by unstable propagation and the formation of a second crack from the second bi-material singularity (IV).

Fig. 11 illustrates the successive failure of specimens of adhesive thickness $t = 24$ mm. Snapshots and the load-displacement curve of one particular specimen shown in the left and center columns, respectively, are representative for 4 out of 5 recorded specimens of this adhesive thickness. Differential (solid lines) and incremental (dashed lines) energy release rates shown in the right column are normalized to $G_c = 3.71$ N/mm such that the initial failure load $F = 846$ N (Fig. 11a) of this particular specimen is recovered by FFM and experimental scatter is accounted for. Crack nucleation is governed by finite fracture mechanics. At the initial failure load the FFM energy criterion is satisfied identically ($\bar{G}/G_c = 1$ at $a = \Delta a$) and associated to a finite crack length of $\Delta a \approx 3$ mm (Fig. 11b). Once a crack is present, the Griffith criterion, Eq. (1), is applicable. At $a = \Delta a$ the differential energy release rate exceeds the fracture toughness, $G > G_c$, and the finite crack $\Delta a$ is unstable while $G/G_c > 1$. As discussed above, $G$ does not increase monotonically but has a distinct local maximum and minimum. Depending on the load level, it may intersect with $G_c$ for $a > \Delta a$. In the present displacement-controlled test crack growth is associated to load reduction. Hence, crack propagation is limited by $G/G_c = 1$ for a loading of $F = 761$ N at point II in the load displacement curve (Fig. 11c). According to Fig. 11d this corresponds to a crack length of $a^+ \approx 16$ mm which agrees well with the experimental observation in frame II at which the initial unstable crack propagation stops. In point II we now find a negative gradient of the differential energy release rate $\partial G/\partial a < 0$ at $G/G_c$. This allows for the experimentally observed stable crack growth from frame II to frame III with increasing applied displacement accompanied by increased loading (Fig. 11e). At a loading of $F = 828$ N at point III ultimate failure and unstable crack growth is observed because here $G/G_c = 1$ corresponds to the local minimum of the curve and the gradient $\partial G/\partial a$ becomes positive again. In Fig. 11f the local minimum is found at $a^{++} \approx 21$ mm for $F = 828$ N. This is in good agreement with the measured crack length prior to ultimate crack propagation in frame III. The considerable load increase after initial and prior to ultimate failure is possible because of the nonmonotonic characteristics of the energy release rate in shear-loaded hyperelastic adhesive joints.

Specimens of $t = 24$ mm adhesive thickness exhibit a significant reduction in transferred loading at initial failure but almost recover the initial load level prior to ultimate failure. Thinner specimens with thickness $t = 12$ mm (Fig. 12) show only a small initial load drop (I–II) and are capable of transferring loads which exceed the initial failure load after crack nucleation (III). The behavior originates from slightly different energy release rate characteristics. Snapshots and load-displacement curves shown in Fig. 12 are representative for 3 out of 4 recorded specimens of adhesive thickness $t = 12$ mm. With a fracture toughness of $G_c = 4.46$ N/mm crack initiation corresponds to $F = 1042$ N and a finite crack length $\Delta a \approx 3$ mm at

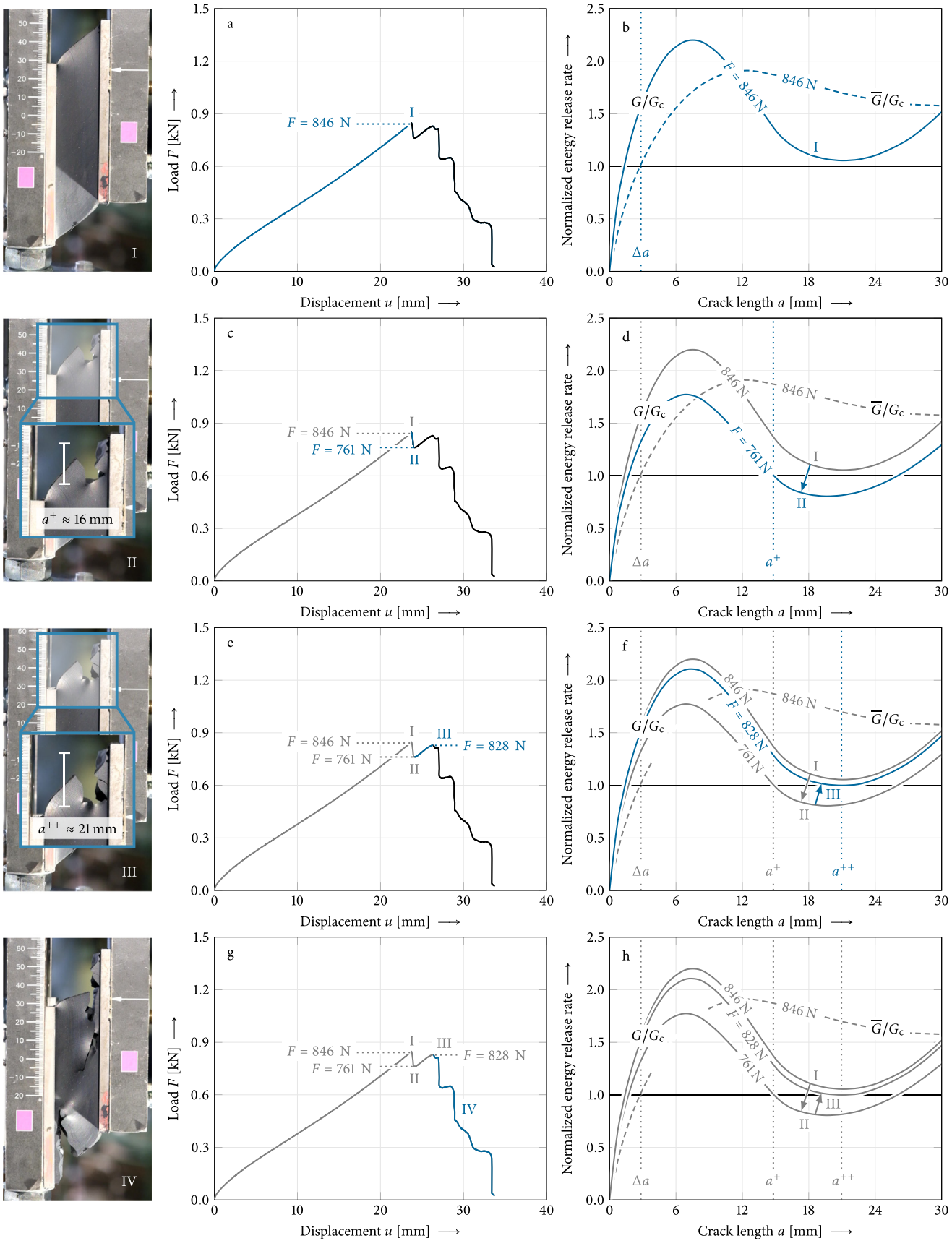


**Fig. 11.** Successive failure of H-shaped specimens of adhesive thickness $t = 24$ mm in simple shear tests: Characteristic experimental snapshots in the left column with corresponding load-displacement curves in the middle column and energy release rates in the right column. Initial failure is accompanied by sudden unstable crack growth, subsequent crack arrest, stable crack growth and finally unstable crack propagation at ultimate loading. Normalized differential and incremental energy release rates $G/G_c$ (solid) and $\bar{G}/G_c$ (dashed), respectively, are shown with $G_c = 3.71$ N/mm accounting for experimental scatter.

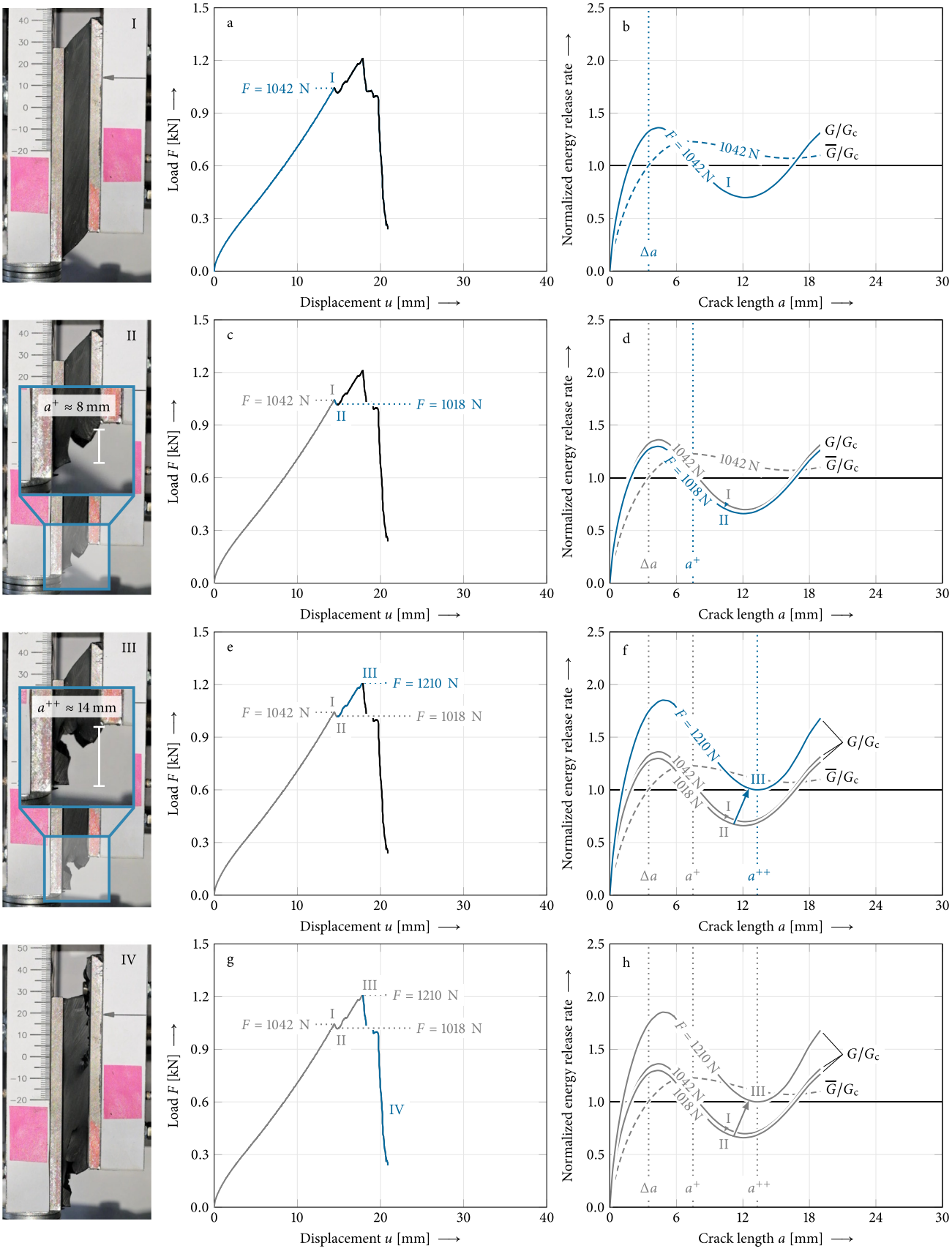


**Fig. 12.** Successive failure of H-shaped specimens of adhesive thickness $t = 12$ mm in simple shear tests: Characteristic experimental snap shots in the left column with corresponding load-displacement curves in the middle column and energy release rates in the right column. Initial failure is accompanied by sudden unstable crack growth, subsequent crack arrest, stable crack growth and finally unstable crack propagation at ultimate loading. Normalized differential and incremental energy release rates $G/G_c$ (solid) and $\overline{G}/G_c$ (dashed), respectively, are shown with $G_c = 4.46$ N/mm accounting for experimental scatter.

$\bar{G}/G_c = 1$ (Fig. 12a and b). Again, the initial crack is unstable while $G/G_c > 1$ (I–II). According to the calculated energy release rates, crack growth stops at $F = 1018$ N and $a^+ \approx 7.5$ mm because $G/G_c = 1$ (Fig. 12c and d). This corresponds well to the experimentally observed crack length $a^+ \approx 8$ mm. Owing to the negative gradient $\partial G/\partial a < 0$ the crack is stable with increasing applied displacement from frame II to III. At the ultimate load $F = 1210$ N $G/G_c$ corresponds to a local minimum followed by unstable crack propagation (Fig. 12e and f). In Fig. 12f this local minimum is found at $a^{++} \approx 13.5$ mm which agrees well with the experimental observation of $a^{++} \approx 14$ mm. The ultimate load of thin $t = 12$ mm adhesive joints exceeds the initial failure load because their energy release rate after initial failure is significantly smaller than the one of $t = 24$ mm joints despite larger transferred loads. This causes unstable crack propagation to stop at shorter lengths $a^+$. Following unstable propagation, a longer relative increase of the crack length, $(a^{++} - a^+)/a^+$, and larger additional loading is required for the local minimum to coincide with $G/G_c = 1$.

The remaining one specimen of adhesive thickness $t = 24$ mm and one specimen of thickness $t = 12$ mm showed the respective other load-displacement characteristics. That is, 1 out of 5 specimens with $t = 24$ mm behaved as shown in Fig. 12 and 1 out of 4 specimens with $t = 12$ mm showed a force-displacement curve as depicted in Fig. 11. However, the observed crack lengths agree with the patterns discussed above. The thinnest specimens of adhesive thickness $t = 6$ mm did not allow for an analysis as above. Crack initiation could only be hardly identified from the recordings. For all three specimens initial failure seemed accompanied by the formation of multiple defects along the entire length of the adhesive.

Our experiments consistently show crack arrest at $a^+_{\min}$ (cf. Fig. 10). Excess energy does not seem become available for crack growth beyond this crack length. In the present case we can conclude $\rho = 0$ for the fraction of excess energy available for crack growth beyond $a^+_{\min}$ introduced by Weißgraeber et al. [56]. It can be assumed that internal damping dissipates excess energy and does not allow strain waves to propagate trough the material.

## 5. Practical implications

Technologically, a sound understanding of the failure processes of silicone adhesives and corresponding physically based failure criteria are needed urgently. For instance, standards defining requirements for structural sealant glazing applications such as the European Technical Approval Guideline for Structural Sealant Glazing Systems, ETAG 002 [51], or the ASTM Standard Guide for Evaluating Failure of Structural Sealant Glazing [82] assume linear elastic material behavior, a simplified load distribution and uniform stresses within the adhesive. They neglect stress concentrations and the nonlinear nature of the adhesive which results in significant design factors to account for all unconsidered effects.

Finite fracture mechanics provides a simple model which intuitively reveals the physics of the fracture process. Involved fundamental material properties – strength or strain hypothesis and fracture toughness – are evident and the presence of a length scale is recognized. The model constitutes a comprehensive tool for the design of efficient and safe components. Yet, in practice fracture mechanical approaches are unpopular because they require knowledge of the energy release rate. Computing energy release rates involves solving several different boundary values problems – one for each considered crack length – which necessitates a certain computational framework.

The present analysis shows that for practical applications of hyperelastic adhesive joints the design methodology can be simplified considerably. Adhesive thicknesses considered in present study correspond to typical applications of DOWSIL™ 993. At these thicknesses the length scale involved in the fracture process remains almost constant across changes of specimen dimensions but also across different joint designs. With a known constant length scale, the coupled criterion, Eq. (6) can be reduced to a pure evaluation of the averaged mixed-mode equivalent strain function at a critical distance $a_c$. The simplified criterion reads

$$\bar{\varepsilon}_{eq}(a_c) = \frac{1}{a_c}\int_0^{a_c} \varepsilon_{eq}(r)\mathrm{d}r = \varepsilon_c,$$
$$\varepsilon_{eq}(r) = \sqrt{2I'_2(r)}\cos\left[\beta\frac{\pi}{6} - \frac{1}{3}\arccos\left(\alpha\,\frac{3\sqrt{3}}{2}\,\frac{I'_3(r)}{I'_2(r)^{3/2}}\right)\right], \qquad (14)$$

where $r$ is the distance from the stress concentration, $\alpha = 0.86$ and $\beta = 1.12$ are shape parameters and $\varepsilon_c = 1.47$ the critical threshold (cf. Fig. 5) identified for DOWSIL™ 993. The design effort simplifies to the evaluation of one boundary value problem using one sufficiently fine FEA. Eq. (14) can be readily implemented in existing finite element codes. Finite crack lengths predicted by FFM in the present analysis are found between approximately 1.5 mm and 2.0 mm (see Figs. 6 and 7). As strains increase towards the bimaterial corner, using a critical distance of $a_c = 1.0$ mm in Eq. (14) will provide conservative predictions of the effective strength of DOWSIL™ 993 adhesive joints. Fig. 13 re-evaluates all joint configurations tested within the present work using Eq. (14). The simplified approach provides accurate yet conservative predictions. The critical distance $a_c$ required for the simplified approach may also be determined experimentally from a best fit of Eq. (14) to test results.

## 6. Conclusion

The present work outlines a framework for the characterization, modeling and design of thick hyperelastic adhesive joints. To this is end, we provide a comprehensive characterization of DOWSIL™ 993 concerning its constitutive behavior and computational modeling. We propose a novel finite fracture mechanics failure model for crack initiation in nonlinear elastic materials. The corresponding coupled criterion combines a mixed-mode strain failure hypothesis of the bulk material based on uniaxial tension, circular shear and biaxial

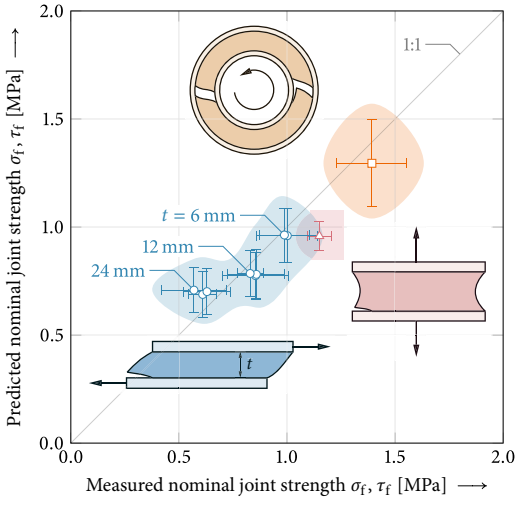


**Fig. 13.** Comparison of predictions obtained using a critical distance of $a_c = 1.0$ mm in Eq. (14) to measured nominal strengths. Error bars on the horizontal axis indicate the experimental standard deviation. Error bars on the vertical axis correspond to predictions using minimum and maximum fracture properties, respectively. Different joint configurations are indicated by their respective color and shaded area.

tension tests with J-integral based measurements of the mode I fracture toughness using DCB specimens. Using a strain criterion instead of the classical stress criterion within the coupled criterion of FFM proves more robust in the case of large deformations.

In order to validate the failure model we tested 77 H-shaped DOWSIL™ 993 specimens under simple shear loading, performed normal plate separation tests of 7 H-shaped specimens and circular shear tests of 4 tubular lap joints. All experiments exhibit considerable scatter. Predictions of the FFM failure model agree with almost all experimental data within 95% confidence intervals accounting for uncertainty of fracture properties. Notably, computed finite crack lengths remain almost constant across different joint designs and dimensional changes. This motivates the proposition of a simplified design methodology for hyperelastic adhesive joints. The simplified approach evaluates only the strain criterion in fixed a critical distance.

Accounting for energetic requirements for crack nucleation, the failure model reproduces and explains size effects such as the adhesive thickness effect. Using a nonlinear crack opening integral, mode I contributions to the energy release rate are shown to cause a nonmonotonic behavior of the total energy release rate. A quantitative analysis of crack lengths, crack initiation and crack propagation reveals that the nonmonotonic energy release rate causes crack arrest and stable crack growth. This effect can allow for an increase of loading after initial failure. The present study considers DOWSIL™ 993 as a representative hyperelastic adhesive. It is expected that results of the present analysis are transferable to other hyperelastic media.

## CRediT authorship contribution statement

**P.L. Rosendahl:** Conceptualization, Data curation, Formal analysis, Investigation, Methodology, Validation, Visualization, Writing - original draft, Writing - review & editing. **Y. Staudt:** Conceptualization, Data curation, Investigation. **A.P. Schneider:** Data curation, Investigation, Validation. **J. Schneider:** Funding acquisition, Supervision, Writing - review & editing. **W. Becker:** Funding acquisition, Supervision, Writing - review & editing.

## Acknowledgments

We are grateful for the support of Christoph Odenbreit with many experiments of the present work. We acknowledge support by the German Research Foundation and the Open Access Publishing Fund of Technische Universität Darmstadt.

## Appendix A. Description of deformation and ultimate extensibility

For the description of ultimate extensibility, a decomposition of the total deformation into its dilatational (change of volume) and distortional (change of shape) parts is essential. Deformation measures derived from the deformation gradient can be decomposed multiplicatively, e.g., $\boldsymbol{F} = J^{1/3}\overline{\boldsymbol{F}}$, where $J = \det \boldsymbol{F}$ is the volume ratio and $\overline{\boldsymbol{F}}$ describes volume-preserving deformations. Using true (logarithmic) strains, the split may be performed additively, which simplifies its mathematical description and geometrical interpretation significantly. For this purpose, consider the log operator

$$\log \boldsymbol{A} := \sum_{i=1}^{n} (\ln \lambda_i) \quad \boldsymbol{n}_i \otimes \boldsymbol{n}_i, \tag{A.1}$$

defining the logarithm of a positive definite matrix $\boldsymbol{A} \in \mathbb{R}^{n\times n}$ where $\lambda_i$ are the (positive) eigenvalues of $\boldsymbol{A}$, $\boldsymbol{n}_i$ are the corresponding (orthonormal) eigenvectors of $\boldsymbol{A}$, ln is the natural logarithm on $\mathbb{R}^+$ and $\otimes$ denotes the outer product: $\boldsymbol{a} \otimes \boldsymbol{b} = \boldsymbol{a}\boldsymbol{b}^{\mathrm{T}}$. Using Eq. (A.1) we can write the spatial Hencky strain tensor as

$$\boldsymbol{H} = \log \boldsymbol{V}, \tag{A.2}$$

where $\boldsymbol{V} = \sqrt{\boldsymbol{F}\boldsymbol{F}^T}$ is the left stretch tensor. The eigenvalues $\varepsilon_i$ of $\boldsymbol{H}$ are principal true (logarithmic) strains

$$\varepsilon_i = \int_{L_i}^{l_i} \frac{\mathrm{d}\tilde{l}}{\tilde{l}} = \ln\left(\frac{l_i}{L_i}\right) = \ln \lambda_i, \quad i = 1,2,3 \quad \text{(no sum)} \tag{A.3}$$

where $L_i$ is the length of a line element in the undeformed reference configuration and $l_i$ the length of the line element in the deformed current configuration. Hence, the Hencky strain tensor may be decomposed according to

$$\begin{aligned} \boldsymbol{H} = \log \boldsymbol{V} &= \log\Bigg[\underbrace{\frac{1}{(\det \boldsymbol{V})^{1/3}}\boldsymbol{V}}_{\substack{\text{distortional,}\\ \text{isochoric}}} \quad \underbrace{(\det \boldsymbol{V})^{1/3}\boldsymbol{I}}_{\substack{\text{dilatational,}\\ \text{volumetric}}}\Bigg] \\ &= \log\left[\frac{1}{(\det \boldsymbol{V})^{1/3}}\boldsymbol{V}\right] + \log\left[(\det \boldsymbol{V})^{1/3}\boldsymbol{I}\right] \\ &= \boldsymbol{H}_{\mathrm{dev}} + \frac{\operatorname{tr}\boldsymbol{H}}{3}\boldsymbol{I}, \end{aligned} \tag{A.4}$$

where $\boldsymbol{I}$ is the identity matrix, $(\operatorname{tr}\boldsymbol{H})\boldsymbol{I}/3$ describes volume change and the deviator $\boldsymbol{H}_{\mathrm{dev}}$ volume-preserving deformations [83].

Isotropy requires invariance of failure criteria with respect to arbitrary rotations of the coordinate system. Therefore, failure criteria may be formulated using invariants of $\boldsymbol{H}_{\mathrm{dev}}$

$$\begin{aligned} I_2' &= \frac{1}{2}\left(\operatorname{tr}\boldsymbol{H}_{\mathrm{dev}}^2 - (\operatorname{tr}\boldsymbol{H}_{\mathrm{dev}})^2\right) \\ &= \frac{1}{6}\left((\varepsilon_1-\varepsilon_2)^2 + (\varepsilon_2-\varepsilon_3)^2 + (\varepsilon_3-\varepsilon_1)^2\right), \end{aligned} \tag{A.5}$$

$$I_3' = \det \boldsymbol{H}_{\mathrm{dev}} = \left(\varepsilon_1 - \frac{1}{3}\operatorname{tr}\boldsymbol{H}\right)\left(\varepsilon_2 - \frac{1}{3}\operatorname{tr}\boldsymbol{H}\right)\left(\varepsilon_3 - \frac{1}{3}\operatorname{tr}\boldsymbol{H}\right), \tag{A.6}$$

where $(\cdot)'$ indicates invariants of the deviatoric part of the Hencky strain tensor.

## Data availability

The raw/processed data required to reproduce these findings are listed in the present manuscript or cited in the reference section where taken from literature.

## References

[1] R.E. Peterson, Methods of correlating data from fatigue tests of stress concentration specimens, Stephen Timoshenko Anniv. Vol., Macmillan, New York, 1938, pp. 179–183.
[2] J.M. Whitney, R.J. Nuismer, Stress fracture criteria for laminated composites containing stress concentrations, J. Compos. Mater. 8 (3) (1974) 253–265. ISSN 0021-9983. https://doi.org/10.1177/002199837400800303.
[3] H. Neuber, Theorie der technischen Formzahl, Forsch. auf dem Gebiete des Ingenieurwesens, 7(6), 1936, pp. 271–274. ISSN 0015-7899. https://doi.org/10.1007/BF02584908.
[4] M.E. Waddoups, J.R. Eisenmann, B.E. Kaminski, Macroscopic fracture mechanics of advanced composite materials, J. Compos. Mater. 5 (4) (1971) 446–454. ISSN 0021-9983. https://doi.org/10.1177/002199837100500402.
[5] Z. Hashin, Finite thermoelastic fracture criterion with application to laminate cracking analysis, J. Mech. Phys. Solids 44 (7) (1996) 1129–1145. ISSN 00225096. https://doi.org/10.1016/0022-5096(95)00080-1.
[6] G.C. Sih, Strain-energy-density factor applied to mixed mode crack problems, Int. J. Fract. 10 (3) (1974) 305–321. ISSN 0376-9429. https://doi.org/10.1007/BF00035493.

[7] P. Lazzarin, R. Zambardi, A finite-volume-energy based approach to predict the static and fatigue behavior of components with sharp V-shaped notches, Int. J. Fract. 112 (3) (2001) 275–298. ISSN 03769429. https://doi.org/10.1023/A:1013595930617.

[8] F. Berto, P. Lazzarin, Recent developments in brittle and quasi-brittle failure assessment of engineering materials by means of local approaches, Mater. Sci. Eng. R Reports 75 (1) (2014) 1–48. ISSN 0927796X. https://doi.org/10.1016/j.mser.2013.11.001.

[9] D. Taylor, The Theory of Critical Distances: A New Perspective in Fracture Mechanics, Elsevier. 2007.ISBN 9780080444789.

[10] G.A. Francfort, J.-J. Marigo, Revisiting brittle fracture as an energy minimization problem, J. Mech. Phys. Solids 46 (8) (1998) 1319–1342. ISSN 00225096. https://doi.org/10.1016/S0022-5096(98)00034-9.

[11] E. Tanné, T. Li, B. Bourdin, J.-J. Marigo, C. Maurini, Crack nucleation in variational phase-field models of brittle fracture, J. Mech. Phys. Solids 110 (2018) 80–99. ISSN 00225096. https://doi.org/10.1016/j.jmps.2017.09.006.

[12] J.-Y. Wu, V.P. Nguyen, A length scale insensitive phase-field damage model for brittle fracture, J. Mech. Phys. Solids 119 (2018) 20–42. ISSN 00225096. https://doi.org/10.1016/j.jmps.2018.06.006.

[13] M. Ortiz, A. Pandolfi, Finite-deformation irreversible cohesive elements for three-dimensional crack-propagation analysis, Int. J. Numer. Methods Eng. 44 (9) (1999) 1267–1282. ISSN 0029-5981. https://doi.org/10.1002/(SICI)1097-0207(19990330)44:9<1267::AID-NME486>3.0.CO;2-7.

[14] T.C. Gasser, G.A. Holzapfel, Modeling 3D crack propagation in unreinforced concrete using PUFEM, Comput. Methods Appl. Mech. Eng. 194 (25-26) (2005) 2859–2896. ISSN 00457825. https://doi.org/10.1016/j.cma.2004.07.025.

[15] H. Ren, X. Zhuang, T. Rabczuk, Dual-horizon peridynamics: a stable solution to varying horizons, Comput. Methods Appl. Mech. Eng. 318 (2017) 762–782. ISSN 00457825. https://doi.org/10.1016/j.cma.2016.12.031.

[16] C.D. Clift, L.D. Carbary, P. Hutley, J.H. Kimberlain, Next generation structural silicone glazing, J. Facade Des. Eng. 2 (3–4) (2014) 137–161. ISSN 2213302X. https://doi.org/10.3233/FDE-150020.

[17] A. Hagl, Development and test logics for structural silicone bonding design and sizing, Glas. Struct. Eng. 1 (1) (2016) 131–151. ISSN 2363-5142. https://doi.org/10.1007/s40940-016-0014-5.

[18] M.R. Ayatollahi, M. Heydari-Meybodi, M. Dehghany, F. Berto, A new criterion for rupture assessment of rubber-like materials under mode-I crack loading: the effective stretch criterion, Adv. Eng. Mater. 18 (8) (2016) 1364–1370. ISSN 15272648. https://doi.org/10.1002/adem.201600046.

[19] M. Heydari-Meybodi, M.R. Ayatollahi, M. Dehghany, F. Berto, Mixed-mode (I/II) failure assessment of rubber materials using the effective stretch criterion, Theor. Appl. Fract. Mech. 91 (2017) 126–133. ISSN 01678442. https://doi.org/10.1016/j.tafmec.2017.05.001.

[20] F. Berto, A criterion based on the local strain energy density for the fracture assessment of cracked and V-notched components made of incompressible hyperelastic materials, Theor. Appl. Fract. Mech. 76 (2015) 17–26. ISSN 01678442. https://doi.org/10.1016/j.tafmec.2014.12.008.

[21] M. Heydari-Meybodi, M.R. Ayatollahi, F. Berto, Rupture analysis of rubber in the presence of a sharp V-shape notch under pure mode-I loading, Int. J. Mech. Sci. 146–147 (2018) 405–415. ISSN 00207403. https://doi.org/10.1016/j.ijmecsci.2018.08.008.

[22] L.-M. Schänzel, H. Dal, C. Miehe, Phase field modeling of fracture in rubbery polymers, Const. Model. Rubber VIII 31 (1975) (2013) 335.

[23] C. Miehe, L.-M. Schänzel, Phase field modeling of fracture in rubbery polymers. Part I: finite elasticity coupled with brittle failure, J. Mech. Phys. Solids 65 (2014) 93–113. ISSN 00225096. https://doi.org/10.1016/j.jmps.2013.06.007.

[24] R.B. Pipes, R.C. Wetherhold, J.W. Gillespie, Notched strength of composite materials, J. Compos. Mater. 13 (2) (1979) 148–160. ISSN 0021-9983. https://doi.org/10.1177/002199837901300206.

[25] D. Leguillon, Strength or toughness? A criterion for crack onset at a notch, Eur. J. Mech. –A/Solids 21 (1) (2002) 61–72. ISSN 09977538. https://doi.org/10.1016/S0997-7538(01)01184-6.

[26] Z. Yosibash, E. Priel, D. Leguillon, A failure criterion for brittle elastic materials under mixed-mode loading, Int. J. Fract. 141 (1-2) (2006) 291–312. ISSN 0376-9429. https://doi.org/10.1007/s10704-006-0083-6.

[27] P. Cornetti, M. Mu noz-Reja, A. Sapora, A. Carpinteri, Finite fracture mechanics and cohesive crack model: weight functions vs. cohesive laws, Int. J. Solids Struct. ISSN 00207683, 10.1016/j.ijsolstr.2018.08.003.

[28] A. Sapora, P. Cornetti, A. Carpinteri, D. Firrao, An improved finite fracture mechanics approach to blunt V-notch brittle fracture mechanics: experimental verification on ceramic, metallic, and plastic materials, Theor. Appl. Fract. Mech. 78 (2015) 20–24. ISSN 01678442. https://doi.org/10.1016/j.tafmec.2015.04.004.

[29] P. Weißgraeber, J. Felger, D. Geipel, W. Becker, Cracks at elliptical holes: stress intensity factor and finite fracture mechanics solution, Eur. J. Mech. - A/Solids 55 (2015) 192–198. ISSN 09977538. https://doi.org/10.1016/j.euromechsol.2015.09.002.

[30] J. Felger, N. Stein, W. Becker, Asymptotic finite fracture mechanics solution for crack onset at elliptical holes in composite plates of finite-width, Eng. Fract. Mech. 182 (2017) 621–634. ISSN 00137944. https://doi.org/10.1016/j.engfracmech.2017.05.048.

[31] A. Talmon l'Armée, S. Hell, P.L. Rosendahl, J. Felger, W. Becker, Nonlinear crack opening integral: mode mixity for finite cracks, Eng. Fract. Mech. 186 (2017) 283–299. ISSN 00137944. https://doi.org/10.1016/j.engfracmech.2017.10.006.

[32] J. Felger, N. Stein, W. Becker, Mixed-mode fracture in open-hole composite plates of finite-width: an asymptotic coupled stress and energy approach, Int. J. Solids Struct. 122-123 (2017) 14–24. ISSN 00207683. https://doi.org/10.1016/j.ijsolstr.2017.05.039.

[33] D. Leguillon, E. Martin, The strengthening effect caused by an elastic contrast –part I: the bimaterial case, Int. J. Fract. 179 (1-2) (2013) 157–167. ISSN 0376-9429. https://doi.org/10.1007/s10704-012-9787-y.

[34] P. Weißgraeber, W. Becker, Finite fracture mechanics model for mixed mode fracture in adhesive joints, Int. J. Solids Struct. 50 (14-15) (2013) 2383–2394. ISSN 00207683. https://doi.org/10.1016/j.ijsolstr.2013.03.012.

[35] S. Hell, P. Weißgraeber, J. Felger, W. Becker, A coupled stress and energy criterion for the assessment of crack initiation in single lap joints: a numerical approach, Eng. Fract. Mech. 117 (2014) 112–126. ISSN 00137944. https://doi.org/10.1016/j.engfracmech.2014.01.012.

[36] N. Stein, P. Weißgraeber, W. Becker, A model for brittle failure in adhesive lap joints of arbitrary joint configuration, Compos. Struct. 133 (2015) 707–718. ISSN 02638223. https://doi.org/10.1016/j.compstruct.2015.07.100.

[37] J. Felger, N. Stein, C. Frey, W. Becker, Scaling laws for the adhesive composite butt joint strength derived by finite fracture mechanics, Compos. Struct. 208 (2019) 546–556. ISSN 02638223. https://doi.org/10.1016/j.compstruct.2018.09.100.

[38] G. Catalanotti, P.P. Camanho, A semi-analytical method to predict net-tension failure of mechanically fastened joints in composite laminates, Compos. Sci. Technol. 76 (2013) 69–76. ISSN 02663538. https://doi.org/10.1016/j.compscitech.2012.12.009.

[39] D. Leguillon, E. Martin, O. Ševeček, R. Bermejo, Application of the coupled stress-energy criterion to predict the fracture behaviour of layered ceramics designed with internal compressive stresses, Eur. J. Mech. - A/Solids 54 (2015) 94–104. ISSN 09977538. https://doi.org/10.1016/j.euromechsol.2015.06.008.

[40] P.L. Rosendahl, P. Weißgraeber, N. Stein, W. Becker, Asymmetric crack onset at open-holes under tensile and in-plane bending loading, Int. J. Solids Struct. 113-114 (2017) 10–23. ISSN 00207683. https://doi.org/10.1016/j.ijsolstr.2016.09.011.

[41] J. Li, E. Martin, D. Leguillon, C. Dupin, A finite fracture model for the analysis of multi-cracking in woven ceramic matrix composites, Compos. Part B Eng. 139 (2018) 75–83. ISSN 13598368. https://doi.org/10.1016/j.compositesb.2017.11.050.

[42] I.G. García, V. Mantič, A. Blázquez, The effect of residual thermal stresses on transverse cracking in cross-ply laminates: an application of the coupled criterion of the finite fracture mechanics, Int. J. Fract. 211 (1-2) (2018) 61–74. ISSN 0376-9429. https://doi.org/10.1007/s10704-018-0276-9.

[43] I.G. García, J. Justo, A. Simon, V. Mantič, Experimental study of the size effect on transverse cracking in cross-ply laminates and comparison with the main theoretical models, Mech. Mater. 128 (September 2018) (2019) 24–37. ISSN 01676636. https://doi.org/10.1016/j.mechmat.2018.09.006.

[44] J. Hebel, R. Dieringer, W. Becker, Modelling brittle crack formation at geometrical and material discontinuities using a finite fracture mechanics approach, Eng. Fract. Mech. 77 (18) (2010) 3558–3572. ISSN 00137944. https://doi.org/10.1016/j.engfracmech.2010.07.005.

[45] A. Doitrand, D. Leguillon, Comparison between 2D and 3D applications of the coupled criterion to crack initiation prediction in scarf adhesive joints, Int. J. Adhes. Adhes. 85 (2018) 69–76. ISSN 01437496. https://doi.org/10.1016/j.ijadhadh.2018.05.022.

[46] A. Doitrand, D. Leguillon, 3D application of the coupled criterion to crack initiation prediction in epoxy/aluminum specimens under four point bending, Int. J. Solids Struct. 143 (2018) 175–182. ISSN 00207683. https://doi.org/10.1016/j.ijsolstr.2018.03.005.

[47] D. Leguillon, E. Martin, O. Ševeček, R. Bermejo, What is the tensile strength of a ceramic to be used in numerical models for predicting crack initiation? Int. J. Fract. 212 (1) (2018) 89–103. ISSN 0376-9429. https://doi.org/10.1007/s10704-018-0294-7.

[48] P. Weißgraeber, D. Leguillon, W. Becker, A review of finite fracture mechanics: crack initiation at singular and non-singular stress raisers, Arch. Appl. Mech. 86 (1-2) (2016) 375–401. ISSN 0939-1533. https://doi.org/10.1007/s00419-015-1091-7.

[49] D. Leguillon, Z. Yosibash, Failure initiation at V-notch tips in quasi-brittle materials, Int. J. Solids Struct. 122-123 (2017) 1–13. ISSN 00207683. https://doi.org/10.1016/j.ijsolstr.2017.05.036.

[50] ASTM Standard D412-16, Standard Test Methods for Vulcanized Rubber and Thermoplastic Elastomers - Tension, ASTM International, West Conshohocken, PA, 2016. ISBN D412-15a. https://doi.org/10.1520/D0412-16.

[51] EOTA, ETAG 002 – European Technical Approval Guideline for Structural Sealant Glazing Systems, European Organization for Technical Approvals EOTA, Brussels, 2012.

[52] ISO 7743, Rubber, vulcanized or thermoplastic – determination of compression stress-strain properties, International Organization for Standardization, Geneva, Switzerland, 2017.

[53] Y. Staudt, C. Odenbreit, J. Schneider, Failure behaviour of silicone adhesive in bonded connections with simple geometry, Int. J. Adhes. Adhes. 82 (2018) 126–138. ISSN 01437496. https://doi.org/10.1016/j.ijadhadh.2017.12.015.

[54] P.L. Rosendahl, M. Drass, J. Felger, J. Schneider, W. Becker, Equivalent strain failure criterion for multiaxially loaded incompressible hyperelastic elastomers, Int. J. Solids Struct. 166 (2019) 32–46. ISSN 00207683. https://doi.org/10.1016/j.ijsolstr.2019.01.030.

[55] J. Felger, P.L. Rosendahl, D. Leguillon, W. Becker, Predicting crack patterns at bimaterial junctions: a coupled stress and energy approach, Int. J. Solids Struct.

164 (2019) 191–201. ISSN 00207683. https://doi.org/10.1016/j.ijsolstr.2019.01.015.
[56] P. Weißgraeber, S. Hell, W. Becker, Crack nucleation in negative geometries, Eng. Fract. Mech. 168 (2016) 93–104. ISSN 00137944. https://doi.org/10.1016/j.engfracmech.2016.02.045.
[57] Y. Staudt, Proposal of a Failure Criterion of Adhesively Bonded Connections With Silicone, Dissertation, University of Luxembourg. 2017.
[58] R.G. Cuntze, Failure conditions for isotropic materials, unidirectional composites, woven fabrics – their visualization and links, Conf. Damage Compos. Mater., 2006, pp. 1–18. Stuttgart.
[59] P.J. Blatz, Application of finite elastic theory to the behavior of rubberlike materials, Rubber Chem. Technol. 36 (5) (1963) 1459–1496. ISSN 0035-9475. https://doi.org/10.5254/1.3539651.
[60] G.H. Lindsey, Triaxial fracture studies, J. Appl. Phys. 38 (12) (1967) 4843. ISSN 00218979. https://doi.org/10.1063/1.1709232.
[61] N. Aït Hocine, A. Hamdi, M. Naït Abdelaziz, P. Heuillet, F. Zaïri, Experimental and finite element investigation of void nucleation in rubber-like materials, Int. J. Solids Struct. 48 (9) (2011) 1248–1254. ISSN 00207683. https://doi.org/10.1016/j.ijsolstr.2011.01.009.
[62] M. Drass, V.A. Kolupaev, J. Schneider, S. Kolling, On cavitation in transparent structural silicone adhesive: TSSA, Glas. Struct. Eng. 3 (2) (2018) 237–256. ISSN 2363-5142. https://doi.org/10.1007/s40940-018-0061-1.
[63] M. Drass, G. Schwind, J. Schneider, S. Kolling, Adhesive connections in glass structures–art I: experiments and analytics on thin structural silicone, Glas. Struct. Eng. 3 (1) (2018) 39–54. ISSN 2363-5142. https://doi.org/10.1007/s40940-017-0046-5.
[64] J. Podgórski, General failure criterion for isotropic media, J. Eng. Mech. 111 (2) (1985) 188–201. ISSN 0733-9399. https://doi.org/10.1061/(ASCE)0733-9399(1985)111:2(188).
[65] D. Bigoni, A. Piccolroaz, Yield criteria for quasibrittle and frictional materials, Int. J. Solids Struct. 41 (11–12) (2004) 2855–2878. ISSN 00207683. https://doi.org/10.1016/j.ijsolstr.2003.12.024.
[66] ASTM Standard D3433-99, Standard test method for fracture strength in cleavage of adhesives in bonded metal joints, ASTM International, West Conshohocken, PA, 2012. ISBN 5935522004. https://doi.org/10.1520/D3433-99R12.2.
[67] BS Standard 7991, Determination of the Mode I Adhesive Fracture Energy, GIc, of Structural Adhesives Using the Double Cantilever Beam (DCB) and Tapered Double Cantilever Beam (TDCB) Specimens, British Standards Institution, London, 2001.
[68] C. Schmandt, S. Marzi, Effect of crack opening velocity and adhesive layer thickness on the fracture behaviour of hyperelastic adhesive joints subjected to mode I loading, Int. J. Adhes. Adhes. 83 (2018) 9–14. ISSN 01437496. https://doi.org/10.1016/j.ijadhadh.2018.02.028.
[69] P.L. Rosendahl, Y. Staudt, C. Odenbreit, J. Schneider, W. Becker, Measuring mode I fracture properties of thick-layered structural silicone sealants, Int. J. Adhes. Adhes. 91 (2019) 64–71. ISSN 01437496. https://doi.org/10.1016/j.ijadhadh.2019.02.012.
[70] L. Loh, S. Marzi, An out-of-plane loaded double cantilever beam (ODCB) test to measure the critical energy release rate in mode III of adhesive joints, Int. J. Adhes. Adhes. 83 (March) (2018) 24–30. ISSN 01437496. https://doi.org/10.1016/j.ijadhadh.2018.02.021.
[71] K. Machalická, M. Eliášová, Adhesive joints in glass structures: effects of various materials in the connection, thickness of the adhesive layer, and ageing, Int. J. Adhes. Adhes. 72 (2017) 10–22. ISSN 01437496. https://doi.org/10.1016/j.ijadhadh.2016.09.007.
[72] Z.-Y. Wang, Y. Shi, Y. Wu, Q. Wang, S. Luo, Shear behaviour of structural silicone adhesively bonded steel-glass orthogonal lap joints, J. Adhes. Sci. Technol. 0 (0) (2018) 1–16. ISSN 0169-4243. https://doi.org/10.1080/01694243.2018.1501862.
[73] A. Moradi, N. Carrère, D. Leguillon, E. Martin, J.-Y. Cognard, Strength prediction of bonded assemblies using a coupled criterion under elastic assumptions: effect of material and geometrical parameters, Int. J. Adhes. Adhes. 47 (2013) 73–82. ISSN 01437496. https://doi.org/10.1016/j.ijadhadh.2013.09.044.
[74] A.S.D. Wang, F.W. Crossman, Initiation and growth of transverse cracks and edge delamination in composite laminates part 1. An energy method, J. Compos. Mater. 14 (1) (1980) 71–87. ISSN 0021-9983. https://doi.org/10.1177/002199838001400106.
[75] R. Krueger, Virtual crack closure technique: history, approach, and applications, Appl. Mech. Rev. 57 (2) (2004) 109. ISSN 00036900. https://doi.org/10.1115/1.1595677.
[76] E. Martin, B. Poitou, D. Leguillon, J.M. Gatt, Competition between deflection and penetration at an interface in the vicinity of a main crack, Int. J. Fract. 151 (2) (2008) 247–268. ISSN 0376-9429. https://doi.org/10.1007/s10704-008-9228-0.
[77] A. Müller, W. Becker, D. Stolten, J. Hohe, A hybrid method to assess interface debonding by finite fracture mechanics, Eng. Fract. Mech. 73 (8) (2006) 994–1008. ISSN 00137944. https://doi.org/10.1016/j.engfracmech.2005.12.001.
[78] I.G. García, V. Mantič, E. Graciani, A model for the prediction of debond onset in spherical-particle-reinforced composites under tension. Application of a coupled stress and energy criterion, Compos. Sci. Technol. 106 (2015) 60–67. ISSN 02663538. https://doi.org/10.1016/j.compscitech.2014.10.010.
[79] A. Doitrand, R. Estevez, D. Leguillon, Comparison between cohesive zone and coupled criterion modeling of crack initiation in rhombus hole specimens under quasi-static compression, Theor. Appl. Fract. Mech. 99 (2019) 51–59. ISSN 01678442. https://doi.org/10.1016/j.tafmec.2018.11.007.
[80] A. Sapora, P. Cornetti, Crack onset and propagation stability from a circular hole under biaxial loading, Int. J. Fract. 214 (1) (2018) 97–104. ISSN 0376-9429. https://doi.org/10.1007/s10704-018-0315-6.
[81] D. Leguillon, E. Martin, The strengthening effect caused by an elastic contrast–art II: stratification by a thin stiff layer, Int. J. Fract. 179 (1-2) (2013) 169–178. ISSN 0376-9429. https://doi.org/10.1007/s10704-012-9785-0.
[82] ASTM Standard C1401-14, Standard Guide for Evaluating Failure of Structural Sealant Glazing, ASTM International, West Conshohocken, PA, 2014. https://doi.org/10.1520/C1401-14.
[83] P. Neff, B. Eidel, R.J. Martin, Geometry of logarithmic strain measures in solid mechanics, Arch. Ration. Mech. Anal. 222 (2) (2016) 507–572. ISSN 14320673. https://doi.org/10.1007/s00205-016-1007-x.